



HAL
open science

The ALMA-PILS survey: First detection of the unsaturated 3-carbon molecules Propenal (C₂H₃CHO) and Propylene (C₃H₆) towards IRAS 16293–2422 B

S. Manigand, A. Coutens, J. -C. Loison, V. Wakelam, H. Calcutt, H. S. P. Müller, J. K. Jørgensen, V. Taquet, S. F. Wampfler, T. L. Bourke, et al.

► To cite this version:

S. Manigand, A. Coutens, J. -C. Loison, V. Wakelam, H. Calcutt, et al.. The ALMA-PILS survey: First detection of the unsaturated 3-carbon molecules Propenal (C₂H₃CHO) and Propylene (C₃H₆) towards IRAS 16293–2422 B. *Astronomy & Astrophysics - A&A*, 2020, <10.1051/0004-6361/202038113>. <hal-02999293>

HAL Id: hal-02999293

<https://hal.science/hal-02999293v1>

Submitted on 29 Mar 2023

HAL is a multi-disciplinary open access archive for the deposit and dissemination of scientific research documents, whether they are published or not. The documents may come from teaching and research institutions in France or abroad, or from public or private research centers.

L'archive ouverte pluridisciplinaire HAL, est destinée au dépôt et à la diffusion de documents scientifiques de niveau recherche, publiés ou non, émanant des établissements d'enseignement et de recherche français ou étrangers, des laboratoires publics ou privés.



HAL Authorization

The ALMA-PILS survey: first detection of the unsaturated 3-carbon molecules Propenal (C_2H_3CHO) and Propylene (C_3H_6) towards IRAS 16293–2422 B

S. Manigand¹, A. Coutens², J.-C. Loison³, V. Wakelam², H. Calcutt⁴, H. S. P. Müller⁵, J. K. Jørgensen¹, V. Taquet⁶, S. F. Wampfler⁷, T. L. Bourke⁸, B. M. Kulterer⁷, E. F. van Dishoeck^{9,10}, M. N. Drozdovskaya⁷, and N. F. W. Ligterink⁷

¹ Niels Bohr Institute & Centre for Star and Planet Formation, University of Copenhagen, Øster Voldgade 5-7, 1350 Copenhagen K., Denmark

e-mail: sebastien@nbi.ku.dk

² Laboratoire d'Astrophysique de Bordeaux, Univ. Bordeaux, CNRS, B18N, allée Geoffroy Saint-Hilaire, 33615 Pessac, France

³ Institut des Sciences Moléculaires (ISM), CNRS, Univ. Bordeaux, 351 cours de la Libération, 33400 Talence, France

⁴ Department of Space, Earth and Environment, Chalmers University of Technology, 41296 Gothenburg, Sweden

⁵ I. Physikalisches Institut, Universität zu Köln, Zùlpicher Str. 77, 50937 Köln, Germany

⁶ INAF, Osservatorio Astrofisico di Arcetri, Largo E. Fermi 5, 50125 Firenze, Italy

⁷ Center for Space and Habitability, University of Bern, Gesellschaftsstrasse 6, 3012 Bern, Switzerland

⁸ SKA Organisation, Jodrell Bank, Lower Withington, Macclesfield, Cheshire SK11 9FT, UK

⁹ Leiden Observatory, Leiden University, PO Box 9513, 2300 RA Leiden, The Netherlands

¹⁰ Max-Planck Institut für Extraterrestrische Physik (MPE), Giessenbachstr. 1, 85748 Garching, Germany

Received 7 April 2020 / Accepted 2 July 2020

ABSTRACT

Context. Complex organic molecules with three carbon atoms are found in the earliest stages of star formation. In particular, propenal (C_2H_3CHO) is a species of interest due to its implication in the formation of more complex species and even biotic molecules.

Aims. This study aims to search for the presence of C_2H_3CHO and other three-carbon species such as propylene (C_3H_6) in the hot corino region of the low-mass protostellar binary IRAS 16293–2422 to understand their formation pathways.

Methods. We use ALMA observations in Band 6 and 7 from various surveys to search for the presence of C_3H_6 and C_2H_3CHO towards the protostar IRAS 16293–2422 B (IRAS 16293B). The identification of the species and the estimates of the column densities and excitation temperatures are carried out by modeling the observed spectrum under the assumption of local thermodynamical equilibrium.

Results. We report the detection of both C_3H_6 and C_2H_3CHO towards IRAS 16293B, however, no blended lines were found towards the other component of the binary system, IRAS 16293A. We derive column density upper limits for C_3H_8 , HCCCCHO, *n*- C_3H_7OH , *i*- C_3H_7OH , C_3O , and *cis*-HC(O)CHO towards IRAS 16293B. We then use a three-phase chemical model to simulate the formation of these species in a typical prestellar environment followed by its hydrodynamical collapse until the birth of the central protostar. Different formation paths, such as successive hydrogenation and radical-radical additions on grain surfaces, are tested and compared to the observational results in a number of different simulations, to assess which are the dominant formation mechanisms in the most embedded region of the protostar.

Conclusions. The simulations reproduce the abundances within one order of magnitude from those observed towards IRAS 16293B, with the best agreement found for a rate of $10^{-12} \text{ cm}^3 \text{ s}^{-1}$ for the gas-phase reaction $C_3 + O \rightarrow C_2 + CO$. Successive hydrogenations of C_3 , HC(O)CHO, and CH_3OCHO on grain surfaces are a major and crucial formation route of complex organic molecules, whereas both successive hydrogenation pathways and radical-radical addition reactions contribute to the formation of C_2H_3CHO .

Key words. astrochemistry – stars: protostars – stars: low-mass – ISM: molecules – ISM: individual objects: IRAS 16293–2422 – submillimeter: ISM

1. Introduction

Aldehyde molecules, which contain a functional group CHO, play an important role in the formation of complex organic molecules (COMs, molecules containing six or more atoms with at least one carbon, Herbst & van Dishoeck 2009). The two-carbon to three-carbon chain aldehydes are generally found in the cold dense regions of star formation as well as in the innermost warm region of protostellar envelope, the hot core. In particular, propenal (C_2H_3CHO), also called acrolein, is considered as a prebiotic species due to its formation after the

decomposition of sugars (Moldoveanu 2010; Bermúdez et al. 2013) and its role in the synthesis of amino acids via Strecker-type reactions (Strecker 1850, 1854) as tested in laboratory studies (e.g. van Trump & Miller 1972; Shibasaki et al. 2008; Grefenstette 2017). On the other hand, on the primordial Earth, C_2H_3CHO is one of a few species that readily reacts with nucleobases of the ribonucleic acid (RNA, Nelsestuen 1980), which makes it a possible sink for the nucleobases and an important hindrance to the start of the RNA world (e.g. Gargaud et al. 2007; Neish et al. 2010). Propynal (HCCCCHO), C_2H_3CHO and propenal (C_2H_5CHO) are suspected to be linked through

their formation on ice surfaces by successive hydrogenation (e.g. Hudson & Moore 1999). C_2H_3CHO and C_2H_5CHO were first detected in the interstellar medium toward the Galactic Center source Sgr B2(N) (Hollis et al. 2004; Requena-Torres et al. 2008), while HCCCHO was first detected towards the dark cloud TMC-1 (Irvine et al. 1988; Turner 1991).

Three-carbon-chain molecules have also been observed in the ISM and are, in general, more abundant towards protostars characterised by warm carbon-chain chemistry (WCCC), such as L1527 (Sakai et al. 2008), and cold dense clouds. For example, propylene (C_3H_6) was detected for the first time towards TMC-1 (Marcelino et al. 2007). It has so far never been reported in warmer environments, where COMs are found with high abundances, such as hot cores/corinos, contrary to methyl acetylene (CH_3CCH) already found with high abundances in such objects (e.g. van Dishoeck et al. 1995; Cazaux et al. 2003).

In this paper we report detections of C_2H_3CHO and C_3H_6 towards the low-mass Class 0 protostellar binary IRAS 16293–2422 (IRAS 16293 hereafter). This source, located in the ρ Ophiuchus cloud complex at a distance of 144 ± 7 pc (Zucker et al. 2019), is well-known as a reference in astrochemistry because of its molecule-rich envelope and the presence of numerous bright emission lines at millimetre wavelengths (for example, van Dishoeck et al. 1995; Cazaux et al. 2003; Caux et al. 2011). The high sensitivity and the high angular resolution of the Atacama Large (sub)Millimeter Array (ALMA) allowed many new detections around solar-type protostars and in the interstellar medium. Using ALMA observations of the Protostellar Interferometric Line Survey (PILS, Jørgensen et al. 2016), some of these new detections of COMs, such as deuterated formamide (NHDCHO and NH_2CDO) and isocyanic acid (HNCO) by Coutens et al. (2016), methyl chloride (CH_3Cl , Fayolle et al. 2017), methyl isocyanate (CH_3NCO , Ligterink et al. 2017), cyanamide (NH_2CN , Coutens et al. 2018a), methyl isocyanide (CH_3NC , Calcutt et al. 2018a), and nitrous acid (HONO, Coutens et al. 2019) have been reported towards this protostellar binary. C_2H_5CHO (Lykke et al. 2017) and CH_3CCH (Calcutt et al. 2019) are also detected in the embedded hot corino towards the “B component” (IRAS 16293B) of this source. This demonstrates the possibility of finding the unsaturated precursors of C_2H_5CHO and provide new constraints on the formation of these species in low-mass protostellar environments. It also suggests the need to develop models to describe these three-carbon species (C_3 -species hereafter) using laboratory measurements and theoretical calculations both for the gas phase and grain surfaces (Loison et al. 2014, 2017; Hickson et al. 2016a; Qasim et al. 2019).

This paper is organised as follows: Sect. 2 describes the observations and the spectroscopic data used in this study. The results and the analysis are presented in Sect. 3. These results are then compared to a chemical model which is described in Sect. 4. Finally, the comparison between the results and the model are discussed in Sect. 5 and the conclusions summarised in Sect. 6.

2. Observations

Observations at 1.3 and 0.8 mm wavelength, carried out with ALMA, corresponding to Band 6 and 7, respectively, towards IRAS 16293 were used in this study. The pointing centre, located between the two protostars of the binary system at $\alpha_{J2000} = 16^h 32^m 22.^s 72$; $\delta_{J2000} = -24^\circ 28' 34''.3$, was the same for all the observations. The species that are the main focus of this study are the C_3 -species C_2H_3CHO and C_3H_6 , as well as the chemically related species HCCCHO, C_2H_5CHO , propanol

(n - C_3H_7OH) and its iso conformer (i - C_3H_7OH), tricarbon monoxide (C_3O), C_3H_8 , and glyoxal (cis- $HC(O)CHO$). Note that the most abundant conformer of $HC(O)CHO$, trans- $HC(O)CHO$, has no dipole moment and does not display any pure rotational transitions, thus it cannot be detected at millimetre wavelengths.

2.1. Band 6 observations

The ALMA-Band 6 data are a combination of PILS observations in Cycle 1 (project-id: 2012.1.00712.S, PI: Jørgensen, J. K.) and Cycle 4 observations taken from Taquet et al. (2018; project-id: 2016.1.01150.S, PI: Taquet, V.). The observations cover a total of ~ 5.5 GHz spread between 221.7 and 250.7 GHz with a frequency resolution of 0.122 MHz, corresponding to a velocity resolution of ~ 0.16 km s $^{-1}$. The two datasets have been treated the same way and were restored with the same $0''.5$ circular beam as in Band 7. The continuum subtraction and the data calibration are detailed in Jørgensen et al. (2016) and Taquet et al. (2018), for Cycle 1 and Cycle 4 observations, respectively. Calibration uncertainties are better than 5% and the sensitivity reached is 1–10 mJy beam $^{-1}$ per channel, depending on the observations.

2.2. Band 7 observations

The Band 7 data are taken from the PILS observations (project-id: 2013.1.00278.S, PI: Jørgensen, J. K.) and cover the full range of 329 to 363 GHz at a frequency resolution of 0.244 MHz, which corresponds to ~ 0.2 km s $^{-1}$ in this frequency range, and were restored with a circular beam of $0''.5$. The continuum subtraction and the data reduction are described in Jørgensen et al. (2016). The sensitivity reaches down to 7–10 mJy beam $^{-1}$ per channel and the relative calibration uncertainty across the band is $\sim 5\%$. Table 1 summarises the details of the spectral windows used in this study.

2.3. Spectroscopic data

The spectroscopic data used to identify C_2H_3CHO transitions are taken from the Cologne Database for Molecular Spectroscopy (CDMS, Müller et al. 2001, 2005). The CDMS entry is based on Daly et al. (2015) with additional data from Winnewisser et al. (1975); Cherniak & Costain (1966). The dipole moment was determined by Blom et al. (1984).

The C_3H_6 rotational transitions are taken from its CDMS entry, based on Craig et al. (2016) with numerous additional transition frequencies from Hirota (1966), Pearson et al. (1994) and Wlodarczak et al. (1994). The dipole moment was measured by Lide & Mann (1957). The spectroscopic entry includes the transitions of A and E torsional substate conformers, which arise from the methyl internal rotation splitting.

Five spectroscopic conformers of n - C_3H_7OH exist, distinguished by the orientation of their methyl and OH groups. Ga- n - C_3H_7OH is the lowest vibrational ground state conformer. The CDMS entry used in this study is largely based on Kisiel et al. (2010), with interactions with other conformers studied by Kahn & Bruice (2005) and additional data from Maeda et al. (2006a); White (1975). The entry only takes the Ga-conformer into account. The correction factor corresponding to the contribution of the other conformers is 2.75 at $T_{ex} = 100$ K.

The CDMS entries for the two conformers *gauche*, the energetically lowest, and *anti* of i - C_3H_7OH are based on Maeda et al. (2006b); Ulenikov et al. (1991); Hirota (1979). Rotation-tunneling interactions between the conformers are incorporated in the Hamiltonian using the formulation described in Christen & Müller (2003). Unlike the n - C_3H_7OH entry, the

Table 1. Observations towards IRAS 16293B used in this study.

Project	Band	Frequency range (GHz)	Spectral resolution (MHz)	Beam size (arcsec)	Sensitivity (mJy beam ⁻¹ channel ⁻¹)
2012.1.00712.S	Band 6	221.77–222.23	0.122	0.5	7–10
		224.7–225.23			
		231.02–231.48			
		232.16–232.62			
		239.42–239.88			
		240.17–240.63			
		247.30–247.76			
2016.1.01150.S	Band 6	233.71–234.18	0.122	0.5	1.2–1.4
		234.92–235.39			
		235.91–236.84			
2013.1.00278.S	Band 7	329.15–362.90	0.244	0.5	7–10

i-C₃H₇OH partition function already includes the contribution of *gauche* and *anti* conformers.

Spectroscopic data of HCCCHO were taken from its CDMS entry, which is based on [McKellar et al. \(2008\)](#) with additional data from [Costain & Morton \(1959\)](#) and [Winnewisser \(1973\)](#). The dipole moment was measured by [Brown & Godfrey \(1984\)](#).

C₃O spectroscopic data are found in the CDMS. The entry is based on the work of [Bizzocchi et al. \(2008\)](#), where they used previous studies and measurements ([Klebsch et al. 1985](#); [Tang et al. 1985](#); [Brown et al. 1983](#)). The dipole moment is reported in the last cited work. The entry does not take the contribution of the torsional/vibrational excited state into account.

C₃H₈ spectroscopic data are taken from the Jet Propulsion Laboratory database (JPL, [Pickett et al. 1998](#)). The JPL entry is based on [Drouin et al. \(2006\)](#), which is a compilation of extensive own data and data taken from [Lide \(1960\)](#), and [Bestmann et al. \(1985a,b\)](#). The partition function includes contributions from the first vibrational and torsional excited states. The dipole moment is reported in [Lide \(1960\)](#).

cis-HC(O)CHO is higher in energy by 1555 ± 48 cm⁻¹ or 2237 ± 69 K than *trans*-HC(O)CHO, however, the latter has no dipole moment thus does not display any rotational transitions. The spectroscopic data are taken from its CDMS entry which is based on the study of [Hübner et al. \(1997\)](#), which also includes the measurement of the dipole moment. Due to the enthalpy difference between *cis* and *trans* conformers, the population fraction of *cis*-HC(O)CHO is 1.9×10^{-10} at 100 K. The abundance derived from the molecular emission of this conformer has to be divided by this factor to retrieve the total abundance of HC(O)CHO.

The main spectroscopic parameters of the different species analysed in this study are summarised in [Table C.1](#).

3. Observational results

For this study we follow the majority of the previous PILS papers and focus on an offset position by 0'.5 in the South-West direction from the most compact source of the binary system, IRAS 16293B (e.g. [Jørgensen et al. 2016](#); [Calcutt et al. 2018b](#); [Ligterink et al. 2017](#)). The spectrum at this position shows narrow lines and is less affected by the strong absorption arising from the continuum emission. At this position the molecular lines have a full width at half-maximum (FWHM) of ~ 1 km s⁻¹ and a velocity peak position (v_{lsr}) of ~ 2.5 – 2.8 km s⁻¹.

3.1. C₃-species lines

A total of 12 unblended lines of C₂H₃CHO have been identified across Bands 6 and 7, with an intensity higher than 3σ —with σ calculated as the root mean square (RMS) of the noise spectrum. 38 other lines that match in terms of frequency were found in the range of the observations. However, they show significant blending with other species. All the lines predicted by the local thermodynamic equilibrium (LTE) model are present in the observations. The upper-level energies of the detected transitions lie between 158 and 401 K, which provide constraints on the excitation temperature. Among these transitions, those at frequencies of 225.192, 330.550 and 336.473 GHz have been used in the fit even though they seem to be slightly blended with other species. All these transitions are listed in [Table E.1](#). C₂H₃CHO has been searched for towards IRAS 16293A as well, however, no lines above 3σ were found, presumably due to the larger linewidth (~ 3 km s⁻¹), and thus the more severe blending, compared to IRAS 16293B.

For C₃H₆, 21 unblended lines were found in the different frequency ranges of the observations. The upper-level energies of the detected transitions lie between 84 and 264 K. 34 lines above 3σ are present in the spectrum, but they are significantly blended with other species, thus they were discarded from the fit. The transition at 349.153 GHz, with an upper-level energy of 355 K, was used in the fit to better assess the excitation temperature, even though the intensity of the line is lower than 3σ . All these transitions are listed in [Table F.1](#). The same lines were found to be completely blended towards IRAS 16293A.

[Figure 1](#) shows the integrated line emission of C₂H₃CHO and C₃H₆. The spatial extent of their emission is marginally resolved and located in the hot corino region, consistently with the other O-bearing COMs detected in the same dataset (e.g. [Jørgensen et al. 2016](#); [Lykke et al. 2017](#); [Calcutt et al. 2018b](#)).

HCCCHO, *n*-C₃H₇OH and *i*-C₃H₇OH, as well as C₃O and *cis*-HC(O)CHO were searched for in the data, however, no line above 1σ was found.

3.2. Column densities

The identification of C₂H₃CHO and C₃H₆ has been confirmed by modelling the molecular emission under the LTE assumption and comparing the spectrum extracted at an offset position from the continuum peak position of IRAS 16293B. The model has

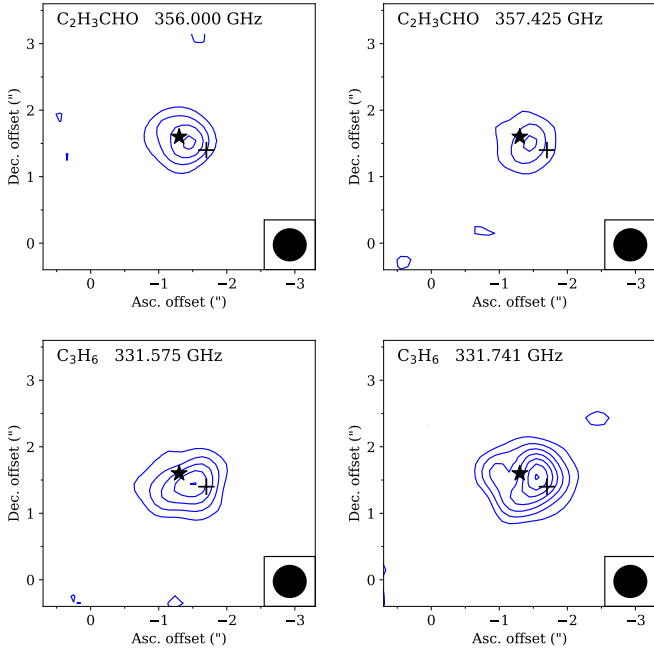


Fig. 1. Integrated intensity maps of the line emission for C_3H_6 and C_2H_3CHO , summed over ± 0.5 MHz. The locations of IRAS 16293B continuum peak and the offset position are marked by the black star and plus sign, respectively. The blue contours start at 4σ and increase by steps of 4σ , where σ is $5 \text{ mJy beam}^{-1} \text{ km s}^{-1}$ for the integrated intensity. A representative beam of 0.5 is shown in the lower right corner of each panel.

been used in Manigand et al. (2020), where more substantial details can be found. This synthetic spectrum considers the gas as a homogeneous slab under LTE conditions and uses the optically thin molecular lines to fit the observed spectrum and to estimate the column density, the rotational temperature, the peak velocity shift, the FWHM and the source size, which is fixed to 0.5 , based on the previous PILS studies.

We run a grid of models in column densities from 10^{13} to 10^{17} cm^{-2} and for excitation temperatures ranging from 50 to 300 K in steps of 25 K. The peak velocity shift and FWHM were set to 2.7 and 0.8 km s^{-1} , respectively, for C_2H_3CHO and 2.5 and 0.8 km s^{-1} , respectively, for C_3H_6 , after a visual inspection of the alignment of the observed lines and the model. The best model was estimated through a χ^2 minimisation, with a modified weighting factor as detailed in Manigand et al. (2020). The modified weighting factor favours the under-estimation of the intensity of the modelled spectrum, which reflects possible unexpected blending effects with other species. A correction factor was applied to the derived column density to take into account the continuum contribution as detailed, for example, in Jørgensen et al. (2018) and Calcutt et al. (2018b). The relative uncertainty of the column density and the rotational temperature is 20%.

The best agreement between the data and the model for C_2H_3CHO was found at an excitation temperature of $125 \pm 25 \text{ K}$ and a column density of $3.4 \pm 0.7 \times 10^{14} \text{ cm}^{-2}$. All the lines used in the fit are shown in Fig. 2. The lower intensity of the lines in Band 7 compared to those in Band 6 emphasises the relatively low rotational temperature derived from the model.

The rotational temperature and column density of C_3H_6 was found to be $75 \pm 15 \text{ K}$ and $4.2 \pm 0.8 \times 10^{16} \text{ cm}^{-2}$, respectively. All the brightest lines in Band 6 are marginally optically thick for the best fit physical conditions. Nevertheless, the optically thick line

at 235.272 GHz shows very good agreement with the observed line, which consolidates the unusually low value of 75 K found for the rotational temperature towards the IRAS 16293B hot corino region. The C_3H_6 lines used to assess the column density and the rotational temperature are shown in Fig. 3.

The majority of C_3H_6 transitions are split into *A* and *E* torsional sub-states due to the CH_3 -group in the molecule. This kind of split is common to most of the species having the CH_3 group, such as CH_3OH or CH_3OCHO . For C_3H_6 , the intensities of the lines at 340.827, 347.774 and 351.738 GHz, corresponding to *E*-transitions, are overestimated by the LTE model. The *A*-transitions that have the same quantum numbers, in particular the same upper-level energies and Einstein's coefficients, are in good agreement with the model. This overestimation of the *E*-transitions alone may suggest that the spin weight ratio between the transitions arising from *A* and *E* substates is not equal to unity.

To test this hypothesis, we added the spin weight of the *E*-transitions with respect to the *A*-transitions in the LTE model and assessed this ratio, given the best fit found for the excitation temperature, velocity shift and FWHM. This spin weight factor $g_{E/A}$ is multiplied to the upper state degeneracy of the *E*-transitions. The best fit was found at the same column density, i.e. $4.2 \pm 0.8 \times 10^{16} \text{ cm}^{-2}$, and a spin weight ratio of $g_{E/A} = 0.6 \pm 0.1$. Figure 4 shows the LTE model, including the discrepancy of the *E*-transitions with respect to the *A*-transitions. This difference between the *A*- and *E*-transitions could reflect an abundance asymmetry between the different conformers, due to low temperature at the moment of their formation, for example. Similar *E/A* ratios were observed towards dark clouds (Friborg et al. 1988), cold prestellar clumps (Menten et al. 1988) and more recently towards young stellar objects (Wirström et al. 2011). Nevertheless, in this study, there are still too few isolated transitions to be able to rule out any bias from the spectroscopic data that could explain this asymmetric *E/A* spin ratio.

For the sake of the chemical modelling comparison, the upper limits on the column density were derived for $HCCCHO$, C_3H_7OH , C_3O , C_3H_8 , and $cis\text{-}HC(O)CHO$. These upper limits correspond to the column density reached in the model when the most intense lines reached 3σ at $\sim 100 \text{ K}$, which is the average excitation temperature of C_2H_3CHO and C_3H_6 . The upper limit of $cis\text{-}HC(O)CHO$ leads to an upper limit of the total amount of $HC(O)CHO$ of $< 2.6 \times 10^{23} \text{ cm}^{-2}$ in the gas phase, which does not provide any real constraint on this molecule. Table 2 summarises the column densities and rotational temperatures of the newly detected species towards source B. Previous detections of chemically related species, namely acetaldehyde (CH_3CHO), acetone (CH_3COCH_3), ethyl methyl ether ($C_2H_5OCH_3$), C_2H_5CHO and CH_3CCH , reported from the same dataset by Lykke et al. (2017) and Calcutt et al. (2019), are also indicated in the table and have been used for a comparison with the chemical model. Qasim et al. (2019) already reported a column density upper limit for $Ga\text{-}n\text{-}C_3H_7OH$ of $< 1.2 \times 10^{15} \text{ cm}^{-2}$ at 300 K and $< 7.4 \times 10^{14} \text{ cm}^{-2}$ at 125 K, using the Band 6 dataset of Taquet et al. (2018). Given their same dataset and the correction factor to include the contribution of the other conformers, this estimate is consistent with the results presented here. In the following, we consider the more conservative column density upper limit of $< 3.0 \times 10^{15} \text{ cm}^{-2}$.

4. The chemical model

In this section, we compare the abundance, and the upper limits, derived from the observations towards IRAS 16293B with

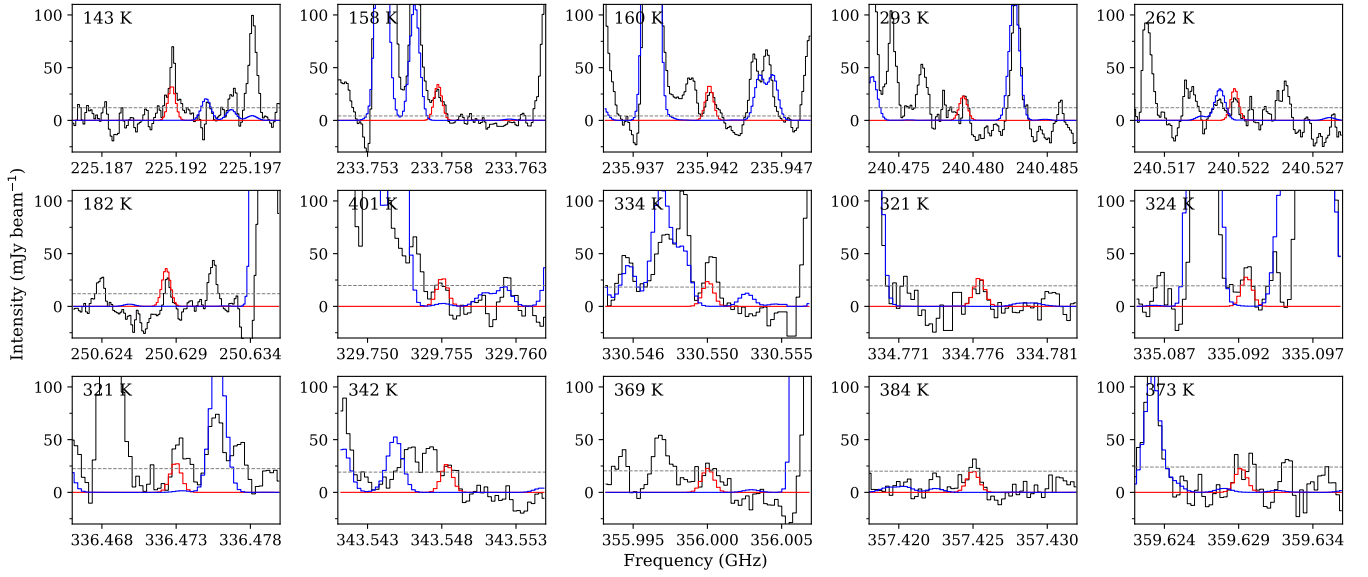


Fig. 2. Identified lines of C_2H_3CHO : the synthetic spectrum, in red, is plotted along with the offset position spectrum towards IRAS 16293B. The straight dashed black line represents the detection limit at the intensity of 3σ . The upper-level energy of the transition is noted in the upper left corner of each panel. The reference spectrum in blue takes the previous species reported in PILS into account (Jørgensen et al. 2016, 2018; Lykke et al. 2017; Coutens et al. 2016; Ligterink et al. 2017; Persson et al. 2018; Calcutt et al. 2018a; Drozdovskaya et al. 2018; Manigand et al. 2019).

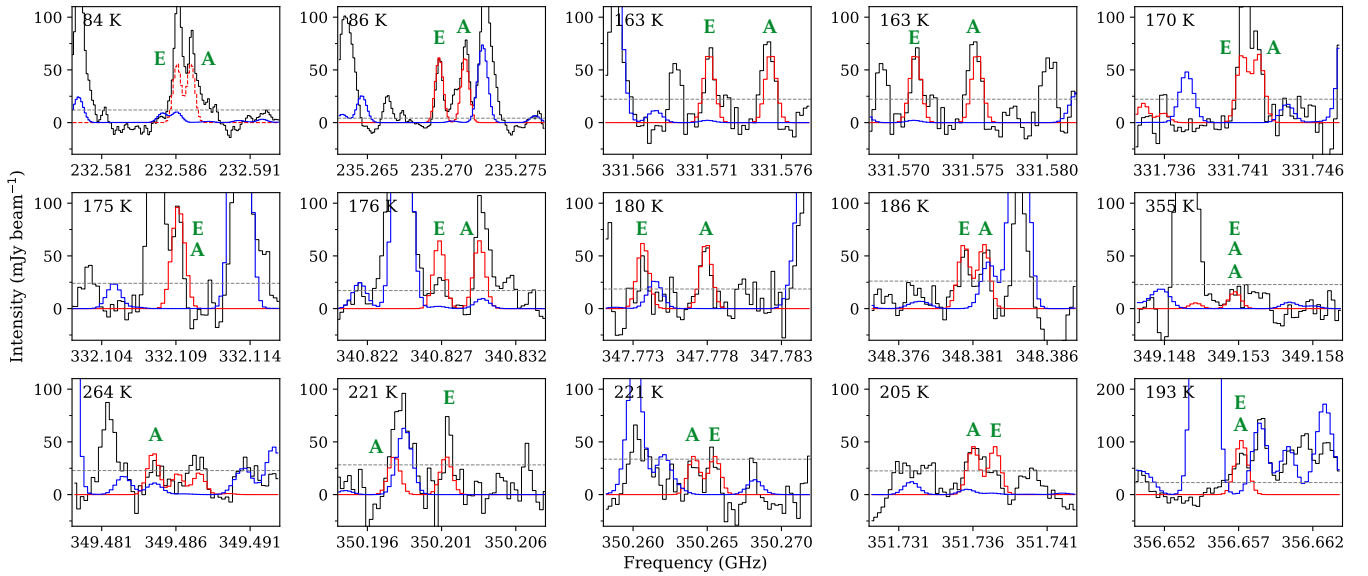


Fig. 3. Identified lines of C_3H_6 : the synthetic spectrum, in red, is plotted along with the offset position spectrum towards IRAS 16293B. The dashed lines correspond to optically thick lines. The straight dashed black line represents the detection limit at the intensity of 3σ . The upper-level energy of the transition is noted in the upper left corner of each panel. The torsional state “E” or “A” of each transition is noted in green on the spectra. The reference spectrum in blue takes the previous species reported in PILS into account (see Fig. 2 and references therein).

a physico-chemical model of a typical low-mass forming star. The core of the simulation uses the Nautilus code (Rauaud et al. 2016), a 3-phase (gas, dust ice surfaces and dust ice mantle) time-dependent chemical model. The chemical study presented here is very similar, in terms of realisation, chemical code and astronomical source, to the studies of Andron et al. (2018) and Coutens et al. (2019). The majority of the differences resides in the extended chemical network used here.

The following subsections present the physical model that describes the evolution of physical conditions of the dust and gas during the simulation, the chemical network that computes the abundance variation caused by the reactions included in the network and the results obtained from the simulations.

4.1. Physical model

Two successive evolutionary stages of a low-mass protostar are simulated: a uniform and constant stage, corresponding to the pre-stellar phase, or the cold-core phase, followed by an evolving stage during which the density and the temperature at the centre of the cloud increases while the envelope is collapsing towards the centre until breaking the hydrostatic equilibrium to form the protostar, i.e. the collapse phase.

The cold-core phase consists of a homogeneous and static cloud at a temperature of 10 K for both gas and dust, a gas density of $2 \times 10^4 \text{ cm}^{-3}$, a visual extinction of 4.5 mag, a cosmic-ray ionisation rate of $1.3 \times 10^{-17} \text{ s}^{-1}$, and a standard external UV

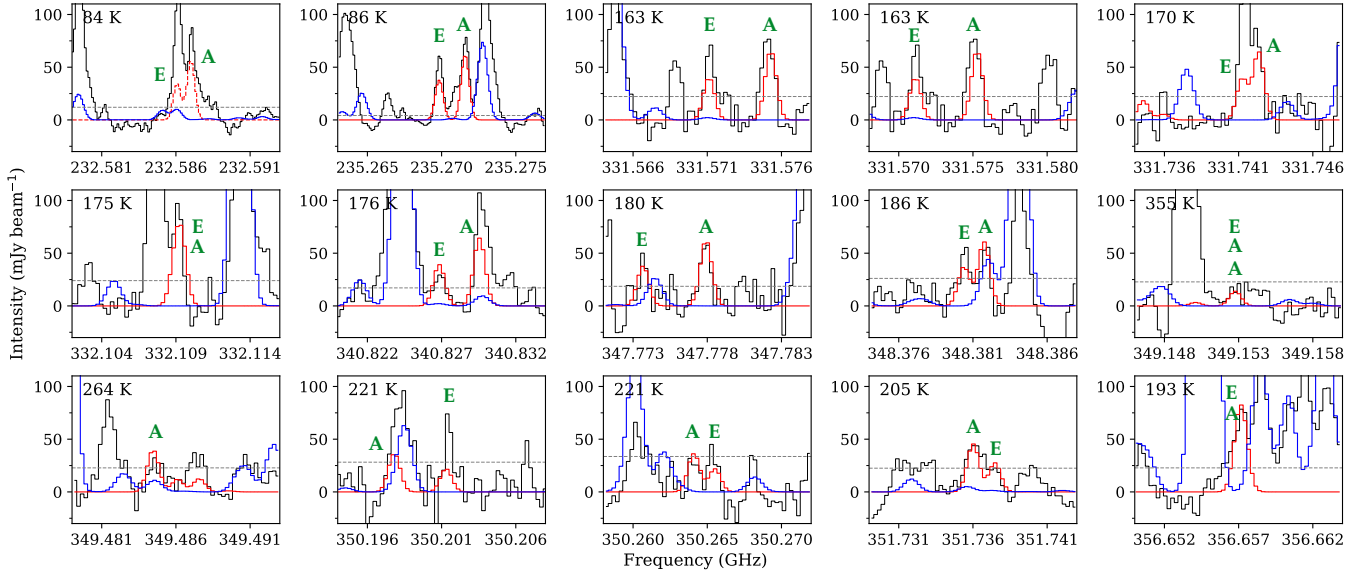


Fig. 4. Identified lines of C_3H_6 synthetic spectrum, in red, including the E/A spin weight ratio of 0.6 ± 0.1 are plotted along with the offset position spectrum towards IRAS 16293B. The dashed lines correspond to optically thick lines. The straight dashed black line represents the detection limit at the intensity of 3σ . The upper-level energy of the transition is noted in the upper left corner of each panel. The torsional state “E” or “A” of each transition is noted in green on the spectra. The reference spectrum in blue takes into account the previous species reported in PILS (see Fig. 2 and reference therein).

Table 2. Column densities of detected species and upper limits of non-detection towards the offset position from IRAS 16293B.

Species	T_{ex} (K)	N_{tot} (cm^{-2})	Ref.
C_2H_3CHO	125 ± 25	$3.4 \pm 0.7 \times 10^{14}$	1
C_3H_6	75 ± 15	$4.2 \pm 0.8 \times 10^{16}$	1
HCCCHO	$100^{(a)}$	$<5.0 \times 10^{14}$	1
$n\text{-}C_3H_7OH$	$100^{(a)}$	$<3.0 \times 10^{15}$	1, 2
$i\text{-}C_3H_7OH$	$100^{(a)}$	$<3.0 \times 10^{15}$	1, 2
C_3O	$100^{(a)}$	$<2.0 \times 10^{13}$	1
cis-HC(O)CHO	$100^{(a)}$	$<5.0 \times 10^{13}$	1
C_3H_8	$100^{(a)}$	$<8.0 \times 10^{16}$	1
CH_3CCH	100 ± 20	$1.1 \pm 0.2 \times 10^{16}$	3
C_2H_5CHO	125 ± 25	$2.2 \pm 1.1 \times 10^{15}$ (\dagger)	4
CH_3CHO	125 ± 25	$7.0 \pm 3.5 \times 10^{16}$ (\dagger)	4
CH_3COCH_3	125 ± 25	$1.7 \pm 0.8 \times 10^{16}$ (\dagger)	4
$C_2H_5OCH_3$	100 ± 20	$1.8 \pm 0.2 \times 10^{16}$ (\dagger)	5

Notes. (\dagger)The authors chose a conservative estimation of the relative uncertainty on the column density of 50%. ($^{(a)}$)The excitation temperature is fixed to the mean excitation temperature of C_2H_3CHO and C_3H_6 and consistent with the excitation temperature of CH_3CCH (Calcutt et al. 2019).

References. (1) This work; (2) Qasim et al. (2019); (3) Calcutt et al. (2019); (4) Lykke et al. (2017); (5) Manigand et al. (2020).

field of $1 G_0$. The collapse phase is the same as used by Aikawa et al. (2008, 2012), Wakelam et al. (2014), Andron et al. (2018), and Coutens et al. (2019). The physical structure used in their study was derived from a 1D radiative hydrodynamical model (Masunaga & Inutsuka 2000), starting from the infall of the cold core, until the collapse stage of the first hydrostatic core, triggered by the dissociation of H_2 by collisions. While the physical structure evolves with time, several parcels of gas are tracked in time and position and their physical properties are traced

Table 3. Initial abundances used in the chemical model.

Species	$n/n(H)$	Species	$n/n(H)$
H_2	5.0×10^{-1}	S^+	1.5×10^{-6}
He	9.0×10^{-2}	Fe^+	1.0×10^{-8}
O	2.4×10^{-4}	F	6.68×10^{-9}
C^+	1.7×10^{-4}	Cl^+	1.0×10^{-9}
N	6.2×10^{-5}		

throughout the collapse. Each parcel ends up at a different radius at the end of the simulation, which allows the evolution of the distribution of the molecular compounds included in the chemical network to be followed. In this study, the chosen parcel of gas starts the collapse at a radius of $>10^4$ au, where it stays for the major part of the collapse and ends-up at a radius of 15 au (see Fig. 5 in Aikawa et al. 2008), where the gas reaches a temperature of ~ 265 K and a density of $4 \times 10^8 \text{ cm}^{-3}$. Figure A.1 shows the evolution of the physical conditions of the targeted parcel of dust and gas. The parcel spends only the last couple of hundred years at a temperature higher than 100 K at a radius <130 au.

4.2. Chemical network

The chemical network includes the kida.uva.2014 gas-grain-phases network as a base (Wakelam et al. 2012, 2015 with updates from Ruaud et al. 2015; Hincelin et al. 2015; Loison et al. 2016, 2017; Hickson et al. 2015, 2016b; Wakelam et al. 2017; Vidal et al. 2017). The initial abundances used in the simulations are listed in Table 3.

Despite the inclusion of dozens of new species, hundred of new reactions, and the inclusion of hundreds of theoretical calculations to determine reaction barriers, there are still large uncertainties on branching ratios due to the lack of experimental studies and the difficulty of determining these branching ratios theoretically. Besides, the diffusion energies of radicals on

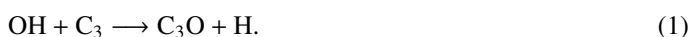
surfaces are not well-known, which again leads to great uncertainties in determining which reactions becomes the most important when the temperature rises. More details on the upgrades made to the chemical network can be found in Appendix B.1.

The chemical model distinguishes the ice surface and the ice mantle during the computation of the chemical reactions and the interaction processes between the different phases. For the comparison with the observations, the ice surface and ice mantle are considered as a single phase. We consequently summed the ice surface and ice mantle abundances to get the total ice abundances. The species in the solid phase are annotated with “s-” in front of their names.

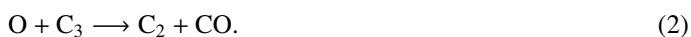
To discuss the formation and destruction paths of the different species, the abundances relative to H₂ have been used in the comparison. This representation is convenient for discussing the evolution of the abundances with the modification of the density and the temperature along with the collapse of the protostellar envelope. The H₂ column density can be derived from the dust continuum radiation, assuming a dust size and an opacity distributions. However, the high continuum absorption seen towards IRAS 16293B in the PILS observations suggests that the dust emission is optically thick. Jørgensen et al. (2016) estimated the lower limit of $>1.2 \times 10^{25} \text{ cm}^{-2}$ for the H₂ column density. Therefore, we chose to use the abundances relative to CH₃OH when comparing the final state of the simulation to the observational results. The abundances derived from the observations are taken from Jørgensen et al. (2016, 2018), Lykke et al. (2017), Manigand et al. (2020) and this study.

4.3. Simulation runs

Different reactions have been considered to reproduce the observations similarly to what has been done in other studies (e.g. Coutens et al. 2018b). Among the important reactions investigated in this paper, the gas-phase formation reaction involving OH is crucial in the formation of C₃O from the consumption of C₃ and has been studied by Loison et al. (2017):



The surface production pathways are marginally contributing to the formation of C₃O radicals present on the ice surfaces, during the pre-stellar phase. The major destructive path of C₃ occurs through the gas-phase reaction:

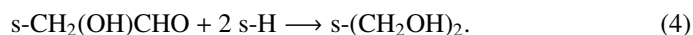
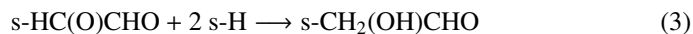


This reaction is thought to play an important role in the abundance of C₃H_x, C₃O, and C₂H_xCHO species (Hickson et al. 2015). The radical-radical addition reactions on grain surfaces are marginally contributing to the final abundances of these complex species.

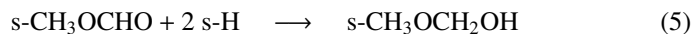
To investigate the chemical network involved in the formation of C₃-species, we run several simulations, depending on the tested chemical branch:

– A1: this simulation is the fiducial model, with which the other models can be compared. The common COMs, such as CH₃OCH₃ and CH₃OCHO, are mainly formed on grain surfaces but gas-phase formation pathways are also included, except for CH₂(OH)CHO, (CH₂OH)₂ and CH₃OCH₂OH. The hydroxyl radical OH contributes only to the formation of C₃O and HCCCHO in the gas phase. A reaction rate of $1.0 \times 10^{-12} \text{ cm}^3 \text{ molecule}^{-1} \text{ s}^{-1}$ is considered for the gas-phase reaction (2).

– B1: the hydrogenation of HC(O)CHO, based on Chuang et al. (2016), has been added to the grain surface reaction network:



In addition, we have included the hydrogenation of CH₃OCHO, forming CH₃OCH₂OH, to the network:



based on the hydrogenation of CH₂(OH)CHO (reaction (3)).

– C1: this run uses the same reaction network as the fiducial run A1. In this case, the pre-stellar phase lasts longer than the other runs, i.e. 3×10^6 yr instead of 1×10^6 yr, which gives the cold chemistry more time to proceed.

– D1: in order to evaluate the contribution rate of the radical-radical addition on the grain surface to the abundance of HCCCHO, C₂H₃CHO and C₂H₅CHO, the following reactions have been removed from the network:



The addition reaction of HCO and C₂H on grains is not contributing to the formation of HCCCHO in our chemical network because the amount of available C₂H on the ice surfaces is limited by the very high activation barrier of the hydrogen abstraction of C₂H₂ ($>56\,000$ K, Zhou et al. 2008).

– E1: this run takes into account the hydrogenation of HC(O)CHO and CH₃OCHO, as it is for run B1, and the activation energies for hydrogenation and abstraction reactions of H₂CO, CH₃OH, C₂H₂, C₂H₄, C₂H₆, C₂H₃CHO, and C₂H₅CHO, taken from the recent laboratory study of Qasim et al. (2019) about propanal and propanol formation on ice surfaces from CO, and the references therein (Andersson et al. 2011; Goumans & Kästner 2011; Kobayashi et al. 2017; Song & Kästner 2017; Álvarez-Barcia et al. 2018; Zaverkin et al. 2018). The activation energies taken from Qasim et al. (2019) are, in general, lower than those used in the simulation runs A1 to D1.

– A2 to E2: these runs are similar to the runs A1 to E1, but with a lower reaction rate of $10^{-16} \text{ cm}^3 \text{ s}^{-1}$ for reaction (2).

The list of the reactions added, extrapolated or removed in each run, with the associated branching ratios and reaction rates, is presented in Appendix B.2. The formation enthalpies of the intermediate species that intervene in the new hydrogenation paths on grain surfaces are taken from Goldsmith et al. (2012).

4.4. Modelling results

The evolution of the abundances during the collapse phase of the run A1 is shown in Fig. 5. For the COMs formed in a hot corino region, most of the molecules targeted are produced on grain surfaces and are released in the gas-phase when the temperature reaches the desorption temperature, between 80 and 130 K depending on the species.

This production scheme leads to a jump of several orders of magnitude in gas-phase abundances of the species around such temperatures. Concerning the C₃-species, the jump in gas-phase abundances is smaller which indicates significant gas-phase

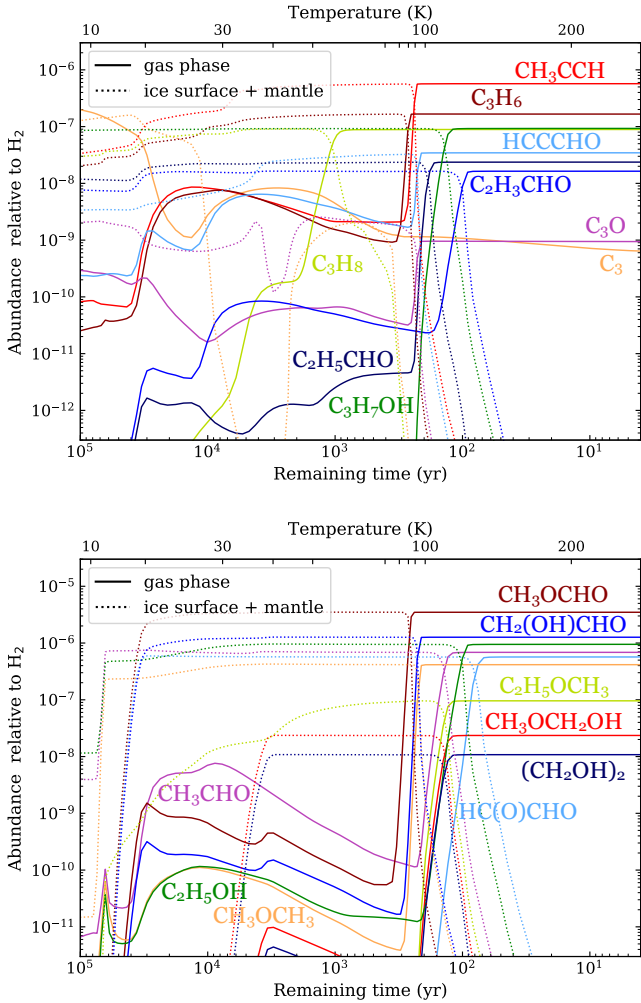


Fig. 5. Time evolution of abundances in the gas phase (solid lines) and on the grain surface (dotted) of several species during the collapse phase of the A1 run. The time axis is reversed to better visualise the abundances evolution. Both panels show the results of the same simulation but with a different selection of species, with their name annotated following the colour code of the curves.

production route contributions. These gas-phase contributions seem higher for the most unsaturated species, such as HCCCHO, C_3 and C_3O . At the end of the simulation, all the formed molecules are in the gas phase.

Figure 6 summarises the gas-phase abundances relative to CH_3OH of the C_3 -species that are under investigation in this study and a few other COMs, such as CH_3OCHO , $CH_2(OH)CHO$, $(CH_2OH)_2$, CH_3OCH_2OH , C_2H_5OH , CH_3COCH_3 , and $C_2H_5OCH_3$, at the end of the collapse phase for every simulation. Because of the assumptions from the physical model compared to the actual physical structure of IRAS 16293B, which is still not perfectly known, an abundance difference of less than one order of magnitude is considered as an agreement between the simulation and the observations.

4.4.1. C_3 -species

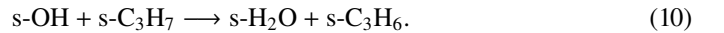
The abundances of C_3 -species, that are CH_3CCH , C_3H_6 , C_3H_8 , HCCCHO, C_2H_3CHO , and C_2H_5CHO , are correlated to those of their precursors, C_3 and C_3O . As C_3 is efficiently produced

and is not a very reactive species in the gas phase, $s-CH_3CCH$ and $s-C_3H_6$ are quite abundant in the solid phase. The comparison between the runs A1–E1 and A2–E2 shows that most of the C_3 -species are sensitive to a decrease in the reaction rate of the C_3 destruction reaction (2). As the reaction rate decreases, there is more C_3 available to form C_3 -species, thus their abundances increase. The increase in the abundances is more pronounced for the more saturated species.

The abundances of the C_3 -species at the end of the simulation run C1 are significantly different from those at the end of the fiducial run. The longer time spent at very low temperatures during the prestellar phase pushes the hydrogenation reactions to produce more saturated C_3 -species by consuming the unsaturated precursors. This is particularly shown by the lower abundances of C_3O and HCCCHO contrasting the higher abundances of C_2H_3CHO and C_2H_5CHO .

The ice-surface formation pathways of C_2H_3CHO and C_2H_5CHO , through reactions (6) and (8), are deactivated in the simulation run D1. The final abundances show a decrease compared to the simulation where the molecules are produced through ice-surface reactions, among others. The updated activation energies, taken from the study of Qasim et al. (2019) and tested in the simulation E1, do not change the final abundances of the C_3 -species significantly.

The C_3H_7OH species is a particular case as there is an alternative production pathway apart from successive hydrogenation of C_3O , mostly the $O + C_3H_8$ reaction. The slight overestimate for C_3H_7OH may be due to an overestimate of the $s-OH + s-C_3H_7$ recombination branching ratio versus the disproportionation, that is the exchange reaction of one H atom from one radical to the other:



Its isomer $C_2H_5OCH_3$, however, is well reproduced by the models, despite the fact that there is only the formation pathway through radical-radical addition that are implemented in the chemical network (see Table B.1). The variation of the final abundance of $C_2H_5OCH_3$ is very similar to that of C_2H_5OH which suggests that they share the same type of formation reactions on ice surfaces, assuming that the major formation pathways of C_2H_5OH effectively take place on ice surfaces as well.

4.4.2. COMs hydrogenation

Concerning the species formed through radical-radical addition, the slight to large overestimation or underestimation of the calculated abundances when considering the fiducial run A1 likely reflects the uncertainties of the association channel branching ratios compared to the disproportionation channel.

The underestimation of $(CH_2OH)_2$ is unexpected considering the large amount of $s-CH_2OH$ as well as the large branching ratio used for the reaction $s-CH_2OH + s-CH_2OH \rightarrow s-(CH_2OH)_2$, that is 50%, in the fiducial chemical network. Despite the approximate agreement between the simulations and the observations for CH_3OCHO and $CH_2(OH)CHO$, these two species are over-produced by the radical-radical additions whereas $(CH_2OH)_2$ and CH_3OCH_2OH , which are only produced by radical-radical additions on grain surfaces, are both under-produced.

The run B1 includes the hydrogenation formation pathways on grain surfaces of $HC(O)CHO$ and CH_3OCHO . These reactions lead to the consumption of the unsaturated species and the

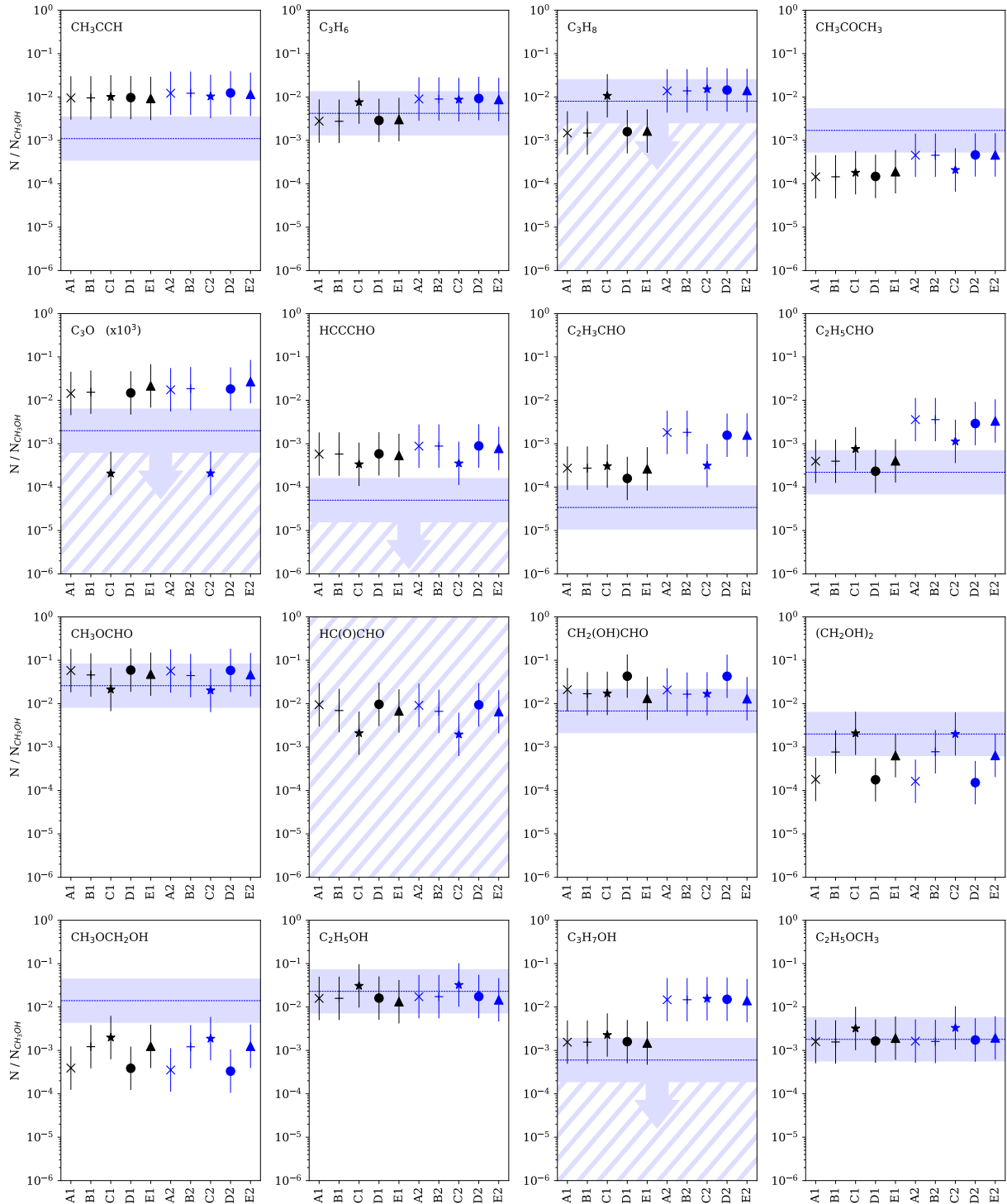


Fig. 6. Final abundances reached at the end of each simulation run for the targeted species. The dashed blue line shows the observed abundance of the species towards IRAS 16293B. The error bars and the blue area correspond to one half order of magnitude confidence limit, thus a 1σ -difference between observations and simulations corresponds to one order of magnitude. The dashed blue region represents the abundance values that are consistent with the corresponding upper limit. The abundance scale of C₃O is lower than the other plots. The abundance upper limit of HC(O)CHO is $<2.6 \times 10^4$ relative to CH₃OH, therefore, there is no observational constraint on the abundance of HC(O)CHO. The abundance upper limit of C₃H₇OH is the sum of n-C₃H₇OH and i-C₃H₇OH abundance upper limits.

production of saturated ones. The agreement of this run with observations is better than for the fiducial chemical network in terms of abundances of CH₂(OH)CHO, (CH₂OH)₂, CH₃OCHO, and CH₃OCH₂OH, suggesting that hydrogenation reactions play an important role in formation of such COMs in hot corino regions. The hydrogenation of CH₃OCHO has been recently

studied in laboratory by [Krim et al. \(2018\)](#). They reported a calculated energy barrier of 32.7 kJ mol^{-1} for the ice-surface reaction s-H + s-CH₃OCHO and concluded that this pathway did not seem to contribute to the formation of CH₃OCH₂OH. The experimental result of Krim et al. mainly shows that this reaction is slower than the s-H + s-H₂CO → s-CH₃O reaction

but does not completely exclude its role in interstellar ice conditions. In our simulation, we include this reaction with a barrier equal to 3000 K (25 kJ mol^{-1}) as average between the value calculated in this work, the value calculated by Krim et al., and the value calculated by [Álvarez-Barcia et al. \(2018\)](#), i.e. 4960 K (41.2 kJ mol^{-1}). This reaction, like all H reactions with barriers, is partly allowed by the tunnel effect.

The reaction $s\text{-HCO} + s\text{-HCO}$ has been suggested to produce $s\text{-HC(O)CHO}$ ([Fedoseev et al. 2015](#); [Chuang et al. 2016](#)) to explain the formation of $\text{CH}_2(\text{OH})\text{CHO}$ and $(\text{CH}_2\text{OH})_2$ in experimental surface hydrogenation of CO molecules. HC(O)CHO production through $s\text{-HCO} + s\text{-HCO}$ reaction is also achieved by [Simons et al. \(2020\)](#) using density functional theory (DFT, [Scuseria & Staroverov 2005](#)) calculations in a model in which the surface molecules were not explicitly taken into account. Additionally, the recent experimental work of [Butscher et al. \(2017\)](#) indicates that the reaction of two HCO radicals on ice surfaces does not lead to HC(O)CHO but rather to H_2CO and CO. Considering the conflicting results from different studies, it is difficult to estimate the proportion of HC(O)CHO produced by the $s\text{-HCO} + s\text{-HCO}$ reaction. In this study, we consider a branching ratio of 5% for HC(O)CHO formation through the $s\text{-HCO} + s\text{-HCO}$ reaction. This leads to a significant production of HC(O)CHO due to the great abundance of HCO on the grains, which is around 1% of the CH_3OH (see Fig. 6). The comparison with the observations is delicate because the most stable isomer of HC(O)CHO , the trans- one, has no dipole moment and the population fraction of cis- HC(O)CHO is equal to 1.9×10^{-10} at 100 K, considering that the thermal equilibrium is reached, and is not detected in the observations.

The updated activation energies from [Qasim et al. \(2019\)](#) of abstraction reactions of CH_3OH and H_2CO affect the final abundances of the COMs that are predominantly formed through radical-radical addition reactions. In particular, the lower final abundance of $(\text{CH}_2\text{OH})_2$ in run E1 compared to B1 is affected by the newly implemented abstraction reaction of CH_3OH which produces CH_3O radicals.

5. Discussion

In most of the models, C_3 reaches a high abundance in the gas phase, due to its low reactivity. This leads to a high abundance of $s\text{-C}_3$ in solid phase, which results in high abundances of all the C_3 -species in the gas phase, especially CH_3CCH , C_3O , and HCCCHO , which are much more abundant than observed. A better agreement to the observations can be found when the rate constant for the $\text{O} + \text{C}_3 \rightarrow \text{C}_2 + \text{CO}$ gas-phase reaction is set to $1 \times 10^{-12} \text{ cm}^3 \text{ s}^{-1}$, assuming a lower activation barrier than in the theoretical work of [Woon & Herbst \(1996\)](#).

The agreement for CH_3CCH , C_3H_6 , $\text{C}_2\text{H}_3\text{CHO}$, and $\text{C}_2\text{H}_5\text{CHO}$ is rather good between the fiducial run A1 and the observations for IRAS 16293. However, this leads to an underestimation of CH_3CCH and C_3H_6 abundances in the case of dense molecular clouds, the agreement being notably less good with observations of TMC-1 ([Marcelino et al. 2007](#); [Markwick et al. 2002](#)) as shown by [Hickson et al. \(2016a\)](#). Alternatively, the abundances of C_3O and HCCCHO are in good agreement with the observations for dense clouds ([Herbst et al. 1984](#); [Irvine et al. 1988](#); [Ohishi & Kaifu 1998](#); [Loison et al. 2016](#)), but they are overproduced for IRAS 16293B. The overproduction of C_3O and HCCCHO for the case of IRAS 16293B may be due to under-represented consumption pathways of these species through ice-surface reactions and demonstrates that laboratory studies in this area are required.

The duration of the prestellar phase has a significant impact on the COM abundances at the end of the simulation. A longer time spent in the prestellar phase enhances the impact of efficient reactions at cold temperature (10 K) on the final abundance. This effect is presumably due to the ongoing hydrogenation at cold temperature, and the addition of nearby radicals, with a non-efficient thermal diffusion on the ice surfaces at a such temperature. The agreement with the observations for C_3H_6 and C_3H_8 is particularly better with a longer prestellar phase in the simulation. The impact on the abundance of $\text{C}_2\text{H}_3\text{CHO}$ and $\text{C}_2\text{H}_5\text{CHO}$ is less important in comparison with the observations.

Concerning the other COMs, a longer prestellar phase leads to a better match of the simulated and observed abundances, in particular for $(\text{CH}_2\text{OH})_2$. The absence of strong outflows from IRAS 16293 B has been suggested as due to this protostar being the less evolved source compared to its companion ([van der Wiel et al. 2019](#)), which shows at least two major outflows ([Yeh et al. 2008](#); [Kristensen et al. 2013](#); [Girart et al. 2014](#)). The abundance ratio of vinyl cyanide ($\text{C}_2\text{H}_3\text{CN}$) and ethyl cyanide ($\text{C}_2\text{H}_5\text{CN}$) observed by [Calcutt et al. \(2018b\)](#) suggests that the warm-up timescale was shorter for IRAS 16293A, the more luminous binary component, or it has a higher accretion rate compared to IRAS 16293B. Another scenario could be that IRAS 16293A started to collapse earlier than IRAS 16293B. This delay of the beginning of the collapse of each protostar of a binary system could be the result of the fragmentation of the parent cloud when the first protostar started to form. This scenario is in agreement with the dynamical modelling study of [Kuffmeier et al. \(2019\)](#), in which the CO-rich bridge structure between the two protostars has been interpreted as a product of the multiple system dynamics and could be a remnant of the parent cloud fragmentation.

The agreement with the observations of the abundance ratios of unsaturated species over saturated ones between the three $\text{C}_2\text{H}_x\text{CHO}$ species is associated with an overall overproduction of these species during the prestellar phase. This overproduction suggests that the common precursors C_3 , and then C_3O , are also overproduced. The over-abundance of C_3 and C_3O could be a result of an underestimation of the consumption of these species by a lack of reactions in the chemical network. The largest carbon-chain species taken into account in the chemical network are C_5H_x in linear forms, and a few benzene-like molecules, such as $\text{C}_6\text{H}_5\text{CN}$, associated to their recent detection in the ISM reported in the study of [McGuire et al. \(2018\)](#). The larger poly-aromatic hydrocarbons (PAH), which are expected to be abundant in space ([Puget & Leger 1989](#)), are not included in the calculation. This limitation in the size of carbon-chain species might be the origin of the over-production, or under-consumption, of the small carbon-chain species, which are the building blocks of these PAHs at cold temperatures as suggested by the recent studies of [Joblin & Cernicharo \(2018\)](#) and [Kaiser et al. \(2015\)](#).

6. Conclusion

This study presents the observations and the chemical modelling of C_3 -species around the Class 0 protostar IRAS 16293B. Using ALMA observations from the PILS survey, the molecular emission is analysed by comparing the spectrum to LTE models to determine the excitation temperatures and column densities of these species. Then, the abundances relative to CH_3OH are compared to the three-phase chemical model Nautilus to investigate the different formation pathways of such molecules under the typical physical conditions of the hot corino region. Different

models were tested, each one focusing on a single aspect of the chemical network. The key findings are summarised in the following:

1. We report the first detection of C₂H₃CHO and C₃H₆ towards the protostar IRAS 16293B. Their emission has an excitation temperature of 125 and 75 K, respectively, and their column densities are found to be $3.4 \pm 0.7 \times 10^{14}$ and $4.2 \pm 0.8 \times 10^{16}$ cm⁻², respectively. These molecules were not detected towards the other member of the binary system. For C₃H₆, the E-transitions were found to exhibit a lower intensity with respect to the A-transitions, leading to a ratio of the E-transitions over A-transitions emitting molecules, being 0.6 ± 0.1 in terms of column densities. The column density upper limits of several chemically related species, that are HCCCHO, C₃H₇OH, C₃O, HC(O)CHO, and C₃H₈, are also reported to provide constraints on the chemical simulations.
2. Most of the simulations reproduce the abundances observed towards IRAS 16293B within an order of magnitude. The final abundances of the different simulations are sensitive to the duration of the prestellar phase, especially when the successive hydrogenation reactions play an important role in the formation of more saturated species. This seems to be the case for CH₃CCH, HC(O)CHO and CH₃OCHO which form C₃H₆, C₃H₈, CH₂(OH)CHO, (CH₂OH)₂ and CH₃OCH₂OH. The longer the cloud spends at low temperatures, the more abundant the saturated species, and the more depleted the precursors.
3. On ice surfaces, the successive hydrogenation reactions of C₃O, forming HCCCHO, C₂H₃CHO, and C₂H₅CHO, and the radical-radical additions of HCO and C₂H₃ or C₂H₅ equally contribute to the amount of C₃-species observed in the hot corino of IRAS 16293B.
4. A high gas-phase reaction rate of 1×10^{-12} cm³ s⁻¹ for the gas-phase reaction C₃ + O → C₂ + CO is necessary to fit the final abundances of C₃-species detected in the observations. The very efficient production of C₃ and C₃O, along with the overall overproduction of C₃-species, suggests that consumption pathways of C₃ species are missing in the chemical network. These chemical routes could be related to the production and growth of PAHs at cold temperatures, which are not included in the present chemical model.

Most of the models reproduce the abundances of the C₃-species towards IRAS 16293B, which emphasises the contribution of the grain-surfaces production pathways under the hot corino physical conditions. Besides, the formation of these species on grain surfaces suggests that they can be incorporated into the protostellar disk as the protostar evolves into a Class I protostar and contribute to the formation of prebiotic molecules. Deeper observations of Class I protostellar disks and the detection of more complex species towards Class I objects are necessary to clearly state on the presence of these molecular species in such objects. Finally, the overproduction of unsaturated C₃-species, in general, suggests the lack of longer carbon-chain molecules formation pathways on grain surfaces and in gas phase and indicate the need of laboratory and theoretical studies of such reactions.

Acknowledgements. The authors thank the referee for useful comments that improved the quality of this manuscript. This paper makes use of the following ALMA data: ADS/JAO.ALMA#2012.1.00712.S, ADS/JAO.ALMA#2013.1.00278.S, and ADS/JAO.ALMA#2016.1.01150.S. ALMA is a partnership of ESO (representing its member states), NSF (USA) and NINS (Japan), together with NRC (Canada), NSC and ASIAA (Taiwan), and KASI (Republic of Korea), in cooperation with the Republic of Chile. The Joint ALMA Observatory is operated by ESO, AUI/NRAO and NAOJ. The group of JKJ acknowledges

support from the H2020 European Research Council (ERC) (grant agreement No 646908) through ERC Consolidator Grant ‘‘S4F’’. Research at Centre for Star and Planet Formation is funded by the Danish National Research Foundation. A.C. acknowledges financial support from the Agence Nationale de la Recherche (grant ANR-19-ERC7-0001-01). S.F.W. acknowledges financial support by the Swiss National Science Foundation (SNSF) Eccellenza Professorial Fellowship PCEFP2_181150. MND and BMK acknowledge the Swiss National Science Foundation (SNSF) Ambizione grant 180079. MND also acknowledges the Center for Space and Habitability (CSH) Fellowship, and the IAU Gruber Foundation Fellowship. This research has made use of NASA’s Astrophysics Data System and VizierR catalogue access tool, CDS, Strasbourg, France (Ochsenbein et al. 2000), as well as community-developed core Python packages for astronomy and scientific computing including Astropy (Astropy Collaboration 2013), Scipy (Jones et al. 2001), Numpy (van der Walt et al. 2011) and Matplotlib (Hunter 2007).

References

- Aikawa, Y., Wakelam, V., Garrod, R. T., & Herbst, E. 2008, *ApJ*, **674**, 984
Aikawa, Y., Wakelam, V., Hersant, F., Garrod, R. T., & Herbst, E. 2012, *ApJ*, **760**, 40
Álvarez-Barcia, S., Russ, P., Kästner, J., & Lamberts, T. 2018, *MNRAS*, **479**, 2007
Andersson, S., Goumans, T. P. M., & Arnaldsson, A. 2011, *Chem. Phys. Lett.*, **513**, 31
Andron, I., Gratier, P., Majumdar, L., et al. 2018, *MNRAS*, **481**, 5651
Ásgeirsson, V., Jónsson, H., & Wikfeldt, K. T. 2017, *J. Phys. Chem. C*, **121**, 1648
Astropy Collaboration (Robitaille, T. P., et al.) 2013, *A&A*, **558**, A33
Baggott, J. E., Frey, H. M., Lightfoot, P. D., & Walsh, R. 1987, *J. Phys. Chem.*, **91**, 3386
Bermúdez, C., Peña, I., Cabezas, C., Daly, A. M., & Alonso, J. L. 2013, *Chem. Phys. Chem.*, **14**, 893
Bestmann, G., Lalowski, W., & Dreizler, H. 1985a, *Zeitschrift Naturforschung Teil A*, **40**, 271
Bestmann, G., Dreizler, H., Vacherand, J. M., et al. 1985b, *Zeitschrift Naturforschung Teil A*, **40**, 508
Bizzocchi, L., Degli Esposti, C., & Dore, L. 2008, *A&A*, **492**, 875
Blom, C. E., Grassi, G., & Bauder, A. 1984, *J. Am. Chem. Soc.*, **106**, 7427
Brown, R. D., & Godfrey, P. D. 1984, *Aust. J. Chem.*, **37**, 1951
Brown, R. D., Eastwood, F. W., Elmes, P. S., & Godfrey, P. D. 1983, *J. Am. Chem. Soc.*, **105**, 6496
Butscher, T., Duvernay, F., Rimola, A., Segado-Centellas, M., & Chiavassa, T. 2017, *Phys. Chem. Chem. Phys.*, **19**, 2857
Calcutt, H., Fiechter, M. R., Willis, E. R., et al. 2018a, *A&A*, **617**, A95
Calcutt, H., Jørgensen, J. K., Müller, H. S. P., et al. 2018b, *A&A*, **616**, A90
Calcutt, H., Willis, E. R., Jørgensen, J. K., et al. 2019, *A&A*, **631**, A137
Caux, E., Kahane, C., Castets, A., et al. 2011, *A&A*, **532**, A23
Cazaux, S., Tielens, A. G. G. M., Ceccarelli, C., et al. 2003, *ApJ*, **593**, L51
Cherniak, E. A., & Costain, C. C. 1966, *J. Chem. Phys.*, **45**, 104
Christen, D., & Müller, H. S. P. 2003, *Phys. Chem. Chem. Phys.*, **5**, 3600
Chuang, K. J., Fedoseev, G., Ioppolo, S., van Dishoeck, E. F., & Linnartz, H. 2016, *MNRAS*, **455**, 1702
Colberg, M., & Friedrichs, G. 2006, *J. Phys. Chem. A*, **110**, 160
Costain, C. C., & Morton, J. R. 1959, *J. Chem. Phys.*, **31**, 389
Coutens, A., Jørgensen, J. K., van der Wiel, M. H. D., et al. 2016, *A&A*, **590**, 1
Coutens, A., Willis, E. R., Garrod, R. T., et al. 2018a, *A&A*, **612**, A107
Coutens, A., Viti, S., Rawlings, J. M. C., et al. 2018b, *MNRAS*, **475**, 2016
Coutens, A., Ligterink, N. F. W., Loison, J. C., et al. 2019, *A&A*, **623**, L13
Craig, N. C., Groner, P., Conrad, A. R., Gurusingham, R., & Tubergen, M. J. 2016, *J. Mol. Spectr.*, **328**, 1
Daly, A. M., Bermúdez, C., Kolesniková, L., & Alonso, J. L. 2015, *ApJS*, **218**, 30
Drouin, B. J., Pearson, J. C., Walters, A., & Lattanzi, V. 2006, *J. Mol. Spectr.*, **240**, 227
Drozdovskaya, M. N., van Dishoeck, E. F., Jørgensen, J. K., et al. 2018, *MNRAS*, **476**, 4949
Enrique-Romero, J., Rimola, A., Ceccarelli, C., & Balucani, N. 2016, *MNRAS*, **459**, L6
Enrique-Romero, J., Álvarez-Barcia, S., Kolb, F. J., et al. 2020, *MNRAS*, **493**, 2523
Fayolle, E. C., Öberg, K. I., Jørgensen, J. K., et al. 2017, *Nat. Astron.*, **1**, 703
Fedoseev, G., Cuppen, H. M., Ioppolo, S., Lamberts, T., & Linnartz, H. 2015, *MNRAS*, **448**, 1288
Friberg, P., Madden, S. C., Hjalmarsen, A., & Irvine, W. M. 1988, *A&A*, **195**, 281

- Gargaud, M., Amils, R., Cernicharo, J., et al. 2007, *Encyclopedia of Astrobiology* (Berlin: Springer-Verlag)
- Garrod, R. T. 2013, *ApJ*, **778**, 158
- Girart, J. M., Estalella, R., Palau, A., Torrelles, J. M., & Rao, R. 2014, *ApJ*, **780**, L11
- Goldsmith, C. F., Magoon, G. R., & Green, W. H. 2012, *J. Phys. Chem. A*, **116**, 9033
- Goumans, T. P. M., & Kästner, J. 2011, *J. Phys. Chem. A*, **115**, 10767
- Grefenstette, N. M. 2017, PhD thesis, University College London, UK
- Herbst, E., & van Dishoeck, E. F. 2009, *ARA&A*, **47**, 427
- Herbst, E., Smith, D., & Adams, N. G. 1984, *A&A*, **138**, L13
- Hickson, K. M., Loison, J.-C., Bourgalais, J., et al. 2015, *ApJ*, **812**, 107
- Hickson, K. M., Wakelam, V., & Loison, J.-C. 2016a, *Mol. Astrophys.*, **3**, 1
- Hickson, K. M., Loison, J.-C., Nuñez-Reyes, D., & Méreau, R. 2016b, *J. Phys. Chem. Lett.*, **7**, 3641
- Hincelin, U., Chang, Q., & Herbst, E. 2015, *A&A*, **574**, A24
- Hirota, E. 1966, *J. Chem. Phys.*, **45**, 1984
- Hirota, E. 1979, *J. Chem. Phys.*, **83**, 1457
- Hollis, J. M., Jewell, P. R., Lovas, F. J., Remijan, A., & Møllendal, H. 2004, *ApJ*, **610**, L21
- Hübner, H., Leeser, A., Burkert, A., Ramsay, D. A., & Hüttner, W. 1997, *J. Mol. Spectr.*, **184**, 221
- Hudson, R. L., & Moore, M. H. 1999, *Icarus*, **140**, 451
- Hunter, J. D. 2007, *Comput. Sci. Eng.*, **9**, 90
- Irvine, W. M., Brown, R. D., Cragg, D. M., et al. 1988, *ApJ*, **335**, L89
- Joblin, C., & Cernicharo, J. 2018, *Science*, **359**, 156
- Jones, E., Oliphant, T., Peterson, P., et al. 2001, SciPy: Open source scientific tools for Python, [Online; accessed January 6, 2021]
- Jørgensen, J. K., van der Wiel, M. H. D., Coutens, A., et al. 2016, *A&A*, **595**, A117
- Jørgensen, J. K., Müller, H. S. P., Calcutt, H., et al. 2018, *A&A*, **620**, A170
- Kahn, K., & Bruice, T. C. 2005, *Chem. Phys. Chem.*, **6**, 487
- Kaiser, R. I., Parker, D. S. N., & Mebel, A. M. 2015, *Ann. Rev. Phys. Chem.*, **66**, 43
- Kisiel, Z., Dorosh, O., Maeda, A., et al. 2010, *Phys. Chem. Chem. Phys.*, **12**, 8329
- Klebsch, W., Bester, M., Yamada, K. M. T., Winnewisser, G., & Joentgen, W. 1985, *A&A*, **152**, L12
- Kobayashi, H., Hidaka, H., Lamberts, T., et al. 2017, *ApJ*, **837**, 155
- Krim, L., Jonas, M., Guillemin, J.-C., Yáñez, M., & Lamsabhi, A. M. 2018, *Phys. Chem. Chem. Phys.*, **20**, 19971
- Krim, L., Guillemin, J.-C., & Woon, D. E. 2019, *MNRAS*, **485**, 5210
- Kristensen, L. E., Klaassen, P. D., Mottram, J. C., Schmalzl, M., & Hogerheijde, M. R. 2013, *A&A*, **549**, L6
- Kuffmeier, M., Calcutt, H., & Kristensen, L. E. 2019, *A&A*, **628**, A112
- Lide, D. R. Jr. 1960, *J. Chem. Phys.*, **33**, 1514
- Lide, D. R. Jr. & Mann, D. E. 1957, *J. Chem. Phys.*, **27**, 868
- Ligterink, N. F. W., Coutens, A., Kofman, V., et al. 2017, *MNRAS*, **469**, 2219
- Loison, J.-C., Wakelam, V., Hickson, K. M., Bergeat, A., & Mereau, R. 2014, *MNRAS*, **437**, 930
- Loison, J.-C., Agúndez, M., Marcelino, N., et al. 2016, *MNRAS*, **456**, 4101
- Loison, J.-C., Agúndez, M., Wakelam, V., et al. 2017, *MNRAS*, **470**, 4075
- Lykke, J. M., Coutens, A., Jørgensen, J. K., et al. 2017, *A&A*, **597**, A53
- Maeda, A., De Lucia, F. C., Herbst, E., et al. 2006a, *ApJS*, **162**, 428
- Maeda, A., Medvedev, I. R., De Lucia, F. C., & Herbst, E. 2006b, *ApJS*, **166**, 650
- Manigand, S., Calcutt, H., Jørgensen, J. K., et al. 2019, *A&A*, **623**, A69
- Manigand, S., Jørgensen, J. K., Calcutt, H., et al. 2020, *A&A*, **635**, A48
- Marcelino, N., Cernicharo, J., Agúndez, M., et al. 2007, *ApJ*, **665**, L127
- Markwick, A. J., Millar, T. J., & Charnley, S. B. 2002, *A&A*, **381**, 560
- Masunaga, H., & Inutsuka, S.-i. 2000, *ApJ*, **536**, 406
- McGuire, B. A., Burkhardt, A. M., Kalenskii, S., et al. 2018, *Science*, **359**, 202
- McKellar, A. R. W., Watson, J. K. G., Chu, L.-K., & Lee, Y.-P. 2008, *J. Mol. Spectr.*, **252**, 230
- Menten, K. M., Walmsley, C. M., Henkel, C., & Wilson, T. L. 1988, *A&A*, **198**, 253
- Moldoveanu, S. 2010, *Pyrolysis of Organic Molecules: Applications to Health and Environmental Issues* (Amsterdam: Elsevier), 28
- Müller, H. S. P., Thorwirth, S., Roth, D. A., & Winnewisser, G. 2001, *A&A*, **370**, L49
- Müller, H. S. P., Schlöder, F., Stutzki, J., & Winnewisser, G. 2005, *J. Mol. Struct.*, **742**, 215
- Neish, C. D., Somogyi, Á., & Smith, M. A. 2010, *Astrobiology*, **10**, 337
- Nelsestuen, G. L. 1980, *J. Mol. Evol.*, **15**, 59
- Ochsenbein, F., Bauer, P., & Marcout, J. 2000, *A&AS*, **143**, 23
- Ohishi, M., & Kaifu, N. 1998, *Faraday Discussions*, **109**, 205
- Pearson, J. C., Sastry, K. V. L. N., Herbst, E., & Delucia, F. C. 1994, *J. Mol. Spectr.*, **166**, 120
- Persson, M. V., Jørgensen, J. K., Müller, H. S. P., et al. 2018, *A&A*, **610**, A54
- Pickett, H. M., Poynter, R. L., Cohen, E. A., et al. 1998, *J. Quant. Spectr. Rad. Transf.*, **60**, 883
- Puget, J. L., & Leger, A. 1989, *ARA&A*, **27**, 161
- Qasim, D., Fedoseev, G., Chuang, K. J., et al. 2019, *A&A*, **627**, A1
- Requena-Torres, M. A., Martín-Pintado, J., Martín, S., & Morris, M. R. 2008, *ApJ*, **672**, 352
- Ruau, M., Loison, J. C., Hickson, K. M., et al. 2015, *MNRAS*, **447**, 4004
- Ruau, M., Wakelam, V., & Hersant, F. 2016, *MNRAS*, **459**, 3756
- Sakai, N., Sakai, T., Hirota, T., & Yamamoto, S. 2008, *ApJ*, **672**, 371
- Scuseria, G. E., & Staroverov, V. N. 2005, in *Theory and Applications of Computational Chemistry*, eds. C. E. Dykstra, G. Frenking, K. S. Kim, & G. E. Scuseria (Amsterdam: Elsevier), 669
- Shibasaki, M., Kanai, M., & Mita, T. 2008, *The Catalytic Asymmetric Strecker Reaction (American Cancer Society)* (Hoboken, NJ: John Wiley), 1
- Simons, M. A. J., Lamberts, T., & Cuppen, H. M. 2020, *A&A*, **634**, A52
- Song, L., & Kästner, J. 2017, *ApJ*, **850**, 118
- Strecker, A. 1850, *Justus Liebigs Annalen der Chemie*, **75**, 27
- Strecker, A. 1854, *Justus Liebigs Annalen der Chemie*, **91**, 349
- Tang, T. B., Inokuchi, H., Saito, S., Yamada, C., & Hirota, E. 1985, *Chem. Phys. Lett.*, **116**, 83
- Taquet, V., van Dishoeck, E. F., Swayne, M., et al. 2018, *A&A*, **618**, A11
- Turner, B. E. 1991, *ApJS*, **76**, 617
- Ulenikov, O. N., Malikova, A. B., Qagar, C. O., et al. 1991, *J. Mol. Spectr.*, **145**, 262
- van der Walt, S., Colbert, S. C., & Varoquaux, G. 2011, *Comput. Sci. Eng.*, **13**, 22
- van der Wiel, M. H. D., Jacobsen, S. K., Jørgensen, J. K., et al. 2019, *A&A*, **626**, A93
- van Trump, J. E., & Miller, S. L. 1972, *Science*, **178**, 859
- van Dishoeck, E. F., Blake, G. A., Jansen, D. J., & Groesbeck, T. D. 1995, *ApJ*, **447**, 760
- Vidal, T. H. G., Loison, J.-C., Jaziri, A. Y., et al. 2017, *MNRAS*, **469**, 435
- Wakelam, V., Herbst, E., Loison, J. C., et al. 2012, *ApJS*, **199**, 21
- Wakelam, V., Vastel, C., Aikawa, Y., et al. 2014, *MNRAS*, **445**, 2854
- Wakelam, V., Loison, J. C., Herbst, E., et al. 2015, *ApJS*, **217**, 20
- Wakelam, V., Loison, J. C., Mereau, R., & Ruau, M. 2017, *Mol. Astrophys.*, **6**, 22
- White, W. F. 1975, Microwave spectra of some volatile organic compounds, Technical report
- Winnewisser, G. 1973, *J. Mol. Spectr.*, **46**, 16
- Winnewisser, M., Winnewisser, G., Honda, T., & Hirota, E. 1975, *Zeitschrift Naturforschung Teil A*, **30**, 1001
- Wirström, E. S., Geppert, W. D., Hjalmarsen, Å., et al. 2011, *A&A*, **533**, A24
- Włodarczak, G., Demaison, J., Heineking, N., & Csaszar, A. G. 1994, *J. Mol. Spectr.*, **167**, 239
- Woon, D. E., & Herbst, E. 1996, *ApJ*, **465**, 795
- Yeh, S. C. C., Hirano, N., Bourke, T. L., et al. 2008, *ApJ*, **675**, 454
- Zaverkin, V., Lamberts, T., Markmeyer, M. N., & Kästner, J. 2018, *A&A*, **617**, A25
- Zhao, Y., & Truhlar, D. G. 2008, *Theor. Chem. Acc.*, **120**, 215
- Zhou, L., Kaiser, R. I., Gao, L. G., et al. 2008, *ApJ*, **686**, 1493
- Zucker, C., Speagle, J. S., Schlafly, E. F., et al. 2019, *ApJ*, **879**, 125

Appendix A: Physical model evolution

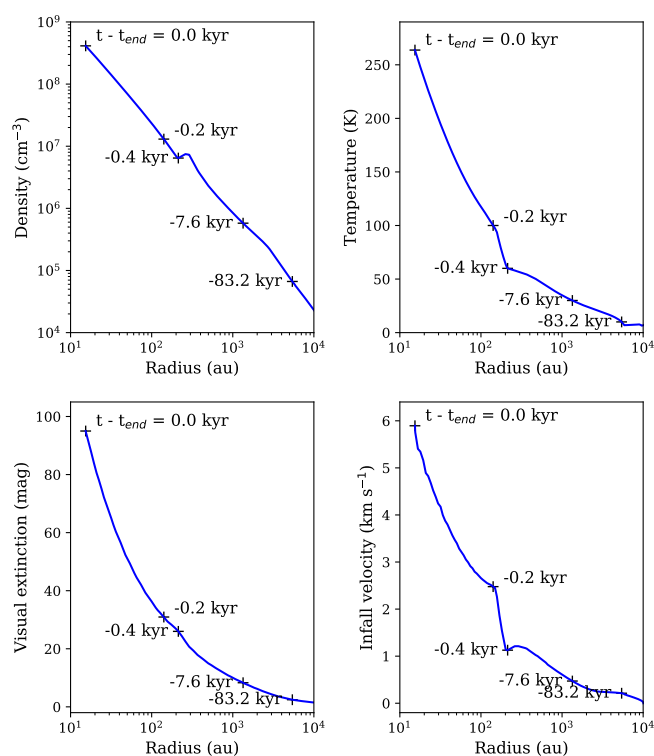


Fig. A.1. Evolution of the density, dust temperature, visual extinction and infall velocity across the envelope during the simulation. The time is indicated at several positions on the curves, with $t = 0$ yr set to the end of the collapse phase in the simulation.

Figure A.1 shows the evolution of the density, the temperature, the extinction coefficient and the infall velocity of the gas during the collapse phase.

Appendix B: Chemical network

B.1. Upgrades from the NAUTILUS public version

The chemical network used here is limited to a skeleton up to five atoms of carbons for linear chains, including oxygen nitrogen and sulfur-bearing, neutral and ionic compounds. Besides, benzene, benzonitrile (C₆H₅CN) and ethylbenzene (C₆H₅C₂H) are also included with their ions. Special care has been taken with end-of-chain processing, which is an important source of error for finite models that want to account for infinite chemistry. In principle, there is no limit for the formation of very large molecules, that are then associated to a very large dilution and thus an abundance of large molecules in most cases very small by bottom-up chemistry. In other words, the limitations are imposed by the extent of the chemical network and the formation of molecules up to five carbons in their structure ensures a proper representation of the production of smaller molecules, such as the C₃-species. Even though there are some notable changes in the gas-phase chemistry (new reactions, update of rate constants and branching ratios according to new measurements and theoretical calculations), the most important changes were made for the grain-surfaces chemistry. The chemistry will be detailed in future articles, thus we only present major changes that concern the species discussed in this work.

We have started to homogenise the chemistry on grains completing the possible reactions for the most abundant species on

grains. First, we systematically supplemented the hydrogenation reactions through s-H and s-H₂ reactions, which are critical because they are favoured by the completion between diffusion and reaction through tunnelling. To estimate the probabilities of the tunnelling effect, we systematically consider a barrier width of 1 Angstrom and we calculate the height of the reaction barriers in the gas phase using the density functional theory (DFT, Scuseria & Staroverov 2005) with the functional M06-2X and the AVTZ basis (Zhao & Truhlar 2008); we have calculated 240 barrier heights for s-H and s-H₂ reactions. The reactions with s-H₂ lead to quick consumption of s-CN, s-OH, s-NH₂, s-C, s-CH, s-CH₂, s-C₂, s-C₂H, s-C₂H₃ as long as there is a lot of s-H₂ on grains. Reactions of these species with s-H₂ are exothermic and are enhanced by tunnelling effect when an activation barrier exists. For some low exothermic reactions, such as s-CH₂ + s-H₂, s-C₂H₃ + s-H₂, and s-NH₂ + s-H₂, a barrier of 1 Angstrom undoubtedly overestimates the tunnelling effect. However, considering the very high abundance of s-H₂, this should not be critical in the end, at least as long as there is a lot of s-H₂ on grains, although more accurate tunnelling treatment would be desirable in the future. We have also modified the Nautilus code to better take into account the tunnelling effect for reactions involving hydrogen atom transfer between heavy species. For example, the O + C₃H₈ → OH + C₃H₇ → C₃H₇OH / C₃H₆ + H₂O reaction is now an efficient source of propanol production through tunnelling of the first step followed by reaction between s-OH and s-C₃H₇ radicals which are supposed to stay close enough on the grains to react. We also consider diffusion by tunneling for all species, with a diffusion barrier width of 2.5 Angstrom according to Ásgeirsson et al. (2017) and a diffusion barrier height equal to 0.6 of the binding energy. The width of the diffusion barrier is not critical as long as it is greater than 2 Angstrom but limits the reactivity through tunnelling for reactions with a high barrier (>5000 K).

We have therefore introduced a large number of reactions involving s-HCO, s-CH₃, s-CH₃O, s-CH₂OH, s-NH, s-HS and to a lesser extent s-H₂NO, s-HNOH, s-H₂CN, s-HCNH, s-CH₃NH, s-CH₂NH₂, s-HOCO, s-H₂NS, s-HNSH, s-C₂H₃, s-C₂H₅, s-C₃H_{x=0-3,5,7} and a few others. For s-CN, s-OH, s-C, s-CH, s-C₂, and s-C₂H we consider a limited number of reactions as these species react with s-H₂. For s-NH₂ and s-CH₂ we consider a relatively large number of reactions even if they can react with H₂ due to their potential role at high temperatures (>20 K) where s-H₂ is low and where their abundance is not negligible due to photodissociation of s-NH₃ and s-CH₄. Of all the possible reactions, those between radicals play an important role in the formation of COMs. As noted already by Garrod (2013), the reaction between two radicals can either lead to a single molecule or to H atom exchange, called disproportionation, for example s-HCO + s-HCO → s-HC(O)CHO or s-H₂CO + s-CO, respectively. The branching ratios are in general poorly known even in the gas phase. Most models favor, when they consider these reactions, formation of the single molecule or use statistical ratios (Garrod 2013). However, when branching ratio determinations exist in the gas phase, it leads to almost exclusively disproportionation except for reactions with CH₃ for which single molecule production is important (Baggott et al. 1987). Moreover, the branching ratios are likely to be significantly different between the gas and grain processes. A recent experimental work (Butscher et al. 2017) suggested that the reaction of two s-HCO radicals on ice surfaces does not lead to HC(O)CHO but rather to s-H₂CO and s-CO. Additionally, Enrique-Romero et al. (2016) found that the interaction between s-HCO and s-CH₃ with water ice (through cluster water ice approximation)

Table B.1. Branching ratios of radical addition reactions.

Reacting species	Produced species	BR (%)	E_a (K)
s-CH ₃ ^(a) + s-CH ₃	→ s-C ₂ H ₆	100	0
s-CH ₃ + s-C ₂ H ₃	→ s-C ₃ H ₆	100	0
	→ s-CH ₄ + s-C ₂ H ₂	0	0
s-CH ₃ + s-C ₂ H ₅	→ s-C ₃ H ₈	100	0
	→ s-CH ₄ + s-C ₂ H ₄	0	0
s-CH ₃ + s-HCO	→ s-CH ₃ CHO	30	0
	→ s-CH ₄ + s-CO	70	0
s-CH ₃ + s-CH ₃ O	→ s-CH ₃ OCH ₃	50	0
	→ s-CH ₄ + s-H ₂ CO	50	0
s-CH ₃ + s-CH ₂ OH	→ s-C ₂ H ₅ OH	30	0
	→ s-CH ₄ + s-H ₂ CO	70	0
s-HCO + s-C ₂ H ₃	→ s-C ₂ H ₃ CHO	10	0
	→ s-C ₂ H ₄ + s-CO	90	0
	→ s-C ₂ H ₂ + s-H ₂ CO	0	0
s-HCO + s-C ₂ H ₅	→ s-C ₂ H ₅ CHO	10	0
	→ s-C ₂ H ₆ + s-CO	90	0
	→ s-C ₂ H ₄ + s-H ₂ CO	0	0
s-HCO + s-HCO	→ s-HC(O)CHO	5	0
	→ s-CO + s-H ₂ CO	95	0
s-HCO + s-CH ₃ O	→ s-CH ₃ OCHO	50	0
	→ s-CO + s-CH ₃ OH	50	0
	→ s-H ₂ CO + s-H ₂ CO	0	0
s-HCO + s-H ₂ CO	→ s-CH ₂ (OH)CHO	5	0
	→ s-CO + s-CH ₃ OH	95	0
	→ s-H ₂ CO + s-H ₂ CO	0	0
s-CH ₃ O + s-CH ₃ O	→ s-CH ₃ OOCH ₃	50	0
	→ s-CH ₃ OH + s-H ₂ CO	50	0
s-CH ₃ O + s-CH ₂ OH	→ s-CH ₃ OCH ₂ OH	50	0
	→ s-CH ₃ OH + s-H ₂ CO	50	0
s-CH ₂ OH + s-CH ₂ OH	→ s-(CH ₂ OH) ₂	50	0
	→ s-CH ₃ OH + s-H ₂ CO	50	0
s-O + s-C ₂ H ₆	→ s-C ₂ H ₅ OH	50	2400
	→ s-H ₂ O + s-C ₂ H ₄	50	2400
s-O + s-C ₃ H ₈	→ s-C ₃ H ₇ OH ^(b)	20	1000
	→ s-H ₂ O + s-C ₃ H ₆	80	1000
s-CH ₃ O + s-C ₂ H ₅	→ s-C ₂ H ₅ OCH ₃	20	0
	→ s-C ₃ OH + s-C ₂ H ₄	20	0
	→ s-H ₂ CO + s-C ₂ H ₆	60	0
s-CH ₃ + s-CH ₃ OCH ₂	→ s-C ₂ H ₅ OCH ₃	100	0

Notes. ^(a)The prefix “s-” means the species is in the solid phase, which corresponds to the ice surface and the ice mantle. ^(b)s-C₃H₇OH accounts for all the isomers.

imposes an initial geometry leading to the formation of s-CH₄ and s-CO through Eley-Rideal reactive mechanism, hindering the formation of s-CH₃CHO at least at low temperatures (~10 K). However, a revision of the model (Enrique-Romero et al. 2020) suggests the possibility to still form s-CH₃CHO through reaction of s-CH₃ and s-HCO. s-CH₃CHO molecules are likely produced at temperatures where s-HCO and s-CH₃ acquire some mobility.

Table B.2. Hydrogenation reactions of CH(O)CHO from Chuang et al. (2016) and CH₃OCHO on grain surfaces.

Reacting species	Produced species	BR (%)
s-H ^(a) + s-HC(O)CHO	→ s-CH(OH)CHO	50
	→ s-CH ₂ (O)CHO	50
s-H + s-CH(OH)CHO	→ s-CH ₂ (OH)CHO	100
s-H + s-CH ₂ (O)CHO	→ s-CH ₂ (OH)CHO	100
s-H + s-CH ₂ (OH)CHO	→ s-CH ₂ (OH)CH ₂ O	50
	→ s-CH ₂ (OH)CHOH	50
s-H + s-CH ₂ (OH)CH ₂ O	→ s-(CH ₂ OH) ₂	100
s-H + s-CH ₂ (OH)CHOH	→ s-(CH ₂ OH) ₂	100
s-H + s-CH ₃ OCHO	→ s-CH ₃ OCH ₂ O	50
	→ s-CH ₃ OCHOH	50
s-H + s-CH ₃ OCH ₂ O	→ s-CH ₃ OCH ₂ OH	100
s-H + s-CH ₃ OCHOH	→ s-CH ₃ OCH ₂ OH	100

Notes. ^(a)The prefix “s-” means the species is in the solid phase, which corresponds to the ice surface and the ice mantle.

In our network, for reactions involving s-CH₃ we always consider a non-negligible branching ratio for the formation of a single molecule deduced from gas-phase measurements. For the radical reactions we largely favour the disproportionation channel except when it is the only effective way to produce some observed species such as CH₃OCHO, which is produced by s-CH₃O + s-HCO on ice surfaces. For the barrier-less addition reactions on unsaturated radicals, such as H + H₂CCCN, we consider addition on several sites due to non-localised radical character of the lonely electron (H₂C=C[•]-C≡N ↔ H₂C=C=C=N[•]) with branching ratios deduced from Mulliken atomic spin density given by theoretical calculations. This leads to nitrile (R-CN) and imine (R=NH) production (Krim et al. 2019), but only low alcohol production in the case of s-H reaction through H atom addition on unsaturated aldehyde radicals (Krim et al. 2018).

The systematic inclusion of reactions between radicals leads to the formation of a very large number of species on grains. We have not systematically completed the chemistry of all the new species, this would lead to an almost infinite number of reactions and species. In a first approach we focused on the most abundant species. For some, but not all of them, we have included the corresponding desorption mechanisms and gas phase chemistry. They are namely C₂H₅CN, C₃H₃CN, HCOCN, C₂H₃CHO, C₂H₅CHO, HC(O)CHO, CH₃COOH, CH₂(OH)CHO and (CH₂OH)₂. At the same time, the gas chemistry of CH₃OCH₃, CH₃COCH₃, C₂H₅OH and C₆H₆ was fully incorporated in the network. Branching ratios used for radicals recombination in this work are summarised in Table B.1. s-*n*-C₃H₇OH is not included in the network by simplification as neither n-C₃H₇OH nor *i*-C₃H₇OH have been firmly detected.

B.2. Discussed reactions

This section presents the list of involved reactions in each run of the chemical simulation. Table B.2 shows the hydrogenation reactions of HC(O)CHO (Chuang et al. 2016) and CH₃OCHO on grain surfaces. The branching ratios have been assumed to be 50% for all the intermediate species. The high reactivity of these species should prevent them from having the time to leave the surface before reacting with another hydrogen atom. Thus, the chemical and physical desorption processes are included

in the network only for the more stable species HC(O)CHO, CH₂(OH)CHO and (CH₂OH)₂. Formation enthalpies of the intermediate species are taken from Goldsmith et al. (2012). Energy barriers of hydrogenation reactions of HC(O)CHO, CH₂(OH)CHO and CH₃OCHO are based on studies of Colberg & Friedrichs (2006), Álvarez-Barcia et al. (2018), Krim et al. (2018) and our calculations. The reactions s-HCO + s-C₂H₃ and s-HCO + s-C₂H₅ that are removed in the runs D1 and D2 are shown in Table B.1.

Appendix C: Main spectroscopic parameters

The main spectroscopic parameters of the species analysed in this paper are shown in Table C.1. It includes the database, the tag number, the dipole moment $\|\mu\|$, the principle axis rotational parameters A , B and C , and the references.

Table C.1. Main spectroscopic parameters of the analysed species.

Species	Database	TAG	$\ \mu\ $ (D)	A (MHz)	B (MHz)	C (MHz)	References
C ₂ H ₃ CHO	CDMS	56519	3.116	47353.71	4659.49	4242.70	1, 2, 3, 4
C ₃ H ₆	CDMS	42516	0.363	46280.29	9305.24	8134.23	5, 6, 7, 8, 9
HCCCHO	CDMS	54510	2.778	68035.30	4826.22	4499.59	10, 11, 12, 13
<i>n</i> -C ₃ H ₇ OH	CDMS	60505	1.415	14330.37	5119.28	4324.23	14, 15, 16, 17
<i>i</i> -C ₃ H ₇ OH	CDMS	60518	1.564	8639.54	8063.22	4768.25	18, 19, 20, 21
C ₃ O	CDMS	52501	2.391	0	4810.89	0	22, 23, 24, 25
cis-HC(O)CHO	CDMS	58513	3.40	26713.36	6190.77	5032.48	26
C ₃ H ₈	JPL	44013	0.085	29207.47	8445.97	7459.00	27, 28, 29, 30

References. (1) Daly et al. (2015); (2) Blom et al. (1984); (3) Winnewisser et al. (1975); (4) Cherniak & Costain (1966); (5) Craig et al. (2016); (6) Wlodarczak et al. (1994); (7) Pearson et al. (1994); (8) Hirota (1966); (9) Lide & Mann (1957); (10) McKellar et al. (2008); (11) Brown & Godfrey (1984); (12) Winnewisser (1973); (13) Costain & Morton (1959); (14) Kisiel et al. (2010); (15) Maeda et al. (2006a); (16) Kahn & Bruice (2005); (17) White (1975); (18) Maeda et al. (2006b); (19) Christen & Müller (2003); (20) Ulenikov et al. (1991); (21) Hirota (1979); (22) Bizzocchi et al. (2008); (23) Klebsch et al. (1985); (24) Tang et al. (1985); (25) Brown et al. (1983); (26) Hübner et al. (1997); (27) Drouin et al. (2006); (28) Bestmann et al. (1985b); (29) Bestmann et al. (1985a); (30) Lide (1960).

Appendix D: Final abundances of the simulation runs

final abundances of the runs while Figs. D.1–D.10 represent the abundance evolution during each simulation run for the studied species.

This appendix section presents the results of the simulations runs for all the relevant species of this study. Table D.1 shows the

Table D.1. Species abundances, relative to CH₃OH, at the end of the collapse phase for all the runs.

Runs / Obs.	Species abundance (relative to CH ₃ OH)							
	CH ₃ CCH	C ₃ H ₆	C ₃ H ₈	C ₃ O	HCCCHO	C ₂ H ₃ CHO	C ₂ H ₅ CHO	C ₃ H ₇ OH ^(a)
PILS	1.1×10^{-3}	4.2×10^{-3}	8.0×10^{-3}	2.0×10^{-6}	5.0×10^{-5}	3.4×10^{-5}	2.2×10^{-4}	6.0×10^{-4}
A1	9.5×10^{-3}	2.8×10^{-3}	1.5×10^{-3}	1.4×10^{-5}	5.8×10^{-4}	2.7×10^{-4}	4.0×10^{-4}	1.5×10^{-3}
B1	9.5×10^{-3}	2.8×10^{-3}	1.5×10^{-3}	1.5×10^{-5}	5.8×10^{-4}	2.7×10^{-4}	4.0×10^{-4}	1.6×10^{-3}
C1	1.0×10^{-2}	7.6×10^{-3}	1.1×10^{-2}	2.1×10^{-7}	3.4×10^{-4}	3.1×10^{-4}	7.6×10^{-4}	2.3×10^{-3}
D1	9.7×10^{-3}	2.9×10^{-3}	1.6×10^{-3}	1.5×10^{-5}	5.9×10^{-4}	1.6×10^{-4}	2.3×10^{-4}	1.6×10^{-3}
E1	9.3×10^{-3}	3.0×10^{-3}	1.6×10^{-3}	2.2×10^{-5}	5.4×10^{-4}	2.6×10^{-4}	4.0×10^{-4}	1.5×10^{-3}
A2	1.2×10^{-2}	9.0×10^{-3}	1.4×10^{-2}	1.8×10^{-5}	8.8×10^{-4}	1.8×10^{-3}	3.6×10^{-3}	1.5×10^{-2}
B2	1.2×10^{-2}	9.0×10^{-3}	1.4×10^{-2}	1.9×10^{-5}	8.8×10^{-4}	1.8×10^{-3}	3.6×10^{-3}	1.5×10^{-2}
C2	1.0×10^{-2}	8.7×10^{-3}	1.5×10^{-2}	2.1×10^{-7}	3.5×10^{-4}	3.1×10^{-4}	1.1×10^{-3}	1.6×10^{-2}
D2	1.2×10^{-2}	9.3×10^{-3}	1.4×10^{-2}	1.8×10^{-5}	8.9×10^{-4}	1.6×10^{-3}	2.9×10^{-3}	1.5×10^{-2}
E2	1.2×10^{-2}	8.7×10^{-3}	1.4×10^{-2}	2.7×10^{-5}	7.8×10^{-4}	1.6×10^{-3}	3.3×10^{-3}	1.4×10^{-2}
	C ₂ H ₅ OH	C ₂ H ₅ OCH ₃	CH ₃ COCH ₃	CH ₃ OCHO	CH ₃ OCH ₂ OH	HC(O)CHO	CH ₂ (OH)CHO	(CH ₂ OH) ₂
PILS	2.3×10^{-2}	1.8×10^{-3}	1.7×10^{-3}	2.6×10^{-2}	1.4×10^{-2}	5.0×10^5	6.8×10^{-3}	2.0×10^{-3}
A1	1.6×10^{-2}	1.6×10^{-3}	1.4×10^{-4}	5.8×10^{-2}	3.9×10^{-4}	9.5×10^{-3}	2.1×10^{-2}	1.8×10^{-4}
B1	1.6×10^{-2}	1.6×10^{-3}	1.5×10^{-4}	4.6×10^{-2}	1.2×10^{-3}	7.0×10^{-3}	1.7×10^{-2}	7.7×10^{-4}
C1	3.1×10^{-2}	3.2×10^{-3}	1.8×10^{-4}	2.1×10^{-2}	2.0×10^{-3}	2.1×10^{-3}	1.7×10^{-2}	2.1×10^{-3}
D1	1.6×10^{-2}	1.6×10^{-3}	1.5×10^{-4}	5.9×10^{-2}	3.9×10^{-4}	9.7×10^{-3}	4.3×10^{-2}	1.8×10^{-4}
E1	1.3×10^{-2}	1.9×10^{-3}	1.9×10^{-4}	4.8×10^{-2}	1.2×10^{-3}	6.8×10^{-3}	1.3×10^{-2}	6.4×10^{-4}
A2	1.7×10^{-2}	1.6×10^{-3}	4.5×10^{-4}	5.7×10^{-2}	3.5×10^{-4}	9.2×10^{-3}	2.1×10^{-2}	1.6×10^{-4}
B2	1.7×10^{-2}	1.6×10^{-3}	4.6×10^{-4}	4.4×10^{-2}	1.2×10^{-3}	6.7×10^{-3}	1.7×10^{-2}	7.8×10^{-4}
C2	3.2×10^{-2}	3.3×10^{-3}	2.1×10^{-4}	2.0×10^{-2}	1.9×10^{-3}	2.0×10^{-3}	1.7×10^{-2}	2.0×10^{-3}
D2	1.7×10^{-2}	1.7×10^{-3}	4.6×10^{-4}	5.9×10^{-2}	3.3×10^{-4}	9.4×10^{-3}	4.3×10^{-2}	1.5×10^{-4}
E2	1.5×10^{-2}	1.9×10^{-3}	4.6×10^{-4}	4.7×10^{-2}	1.2×10^{-3}	6.6×10^{-3}	1.3×10^{-2}	6.4×10^{-4}

Notes. ^(a)C₃H₇OH abundance for the PILS observations is the sum of the abundance of all the isomers.

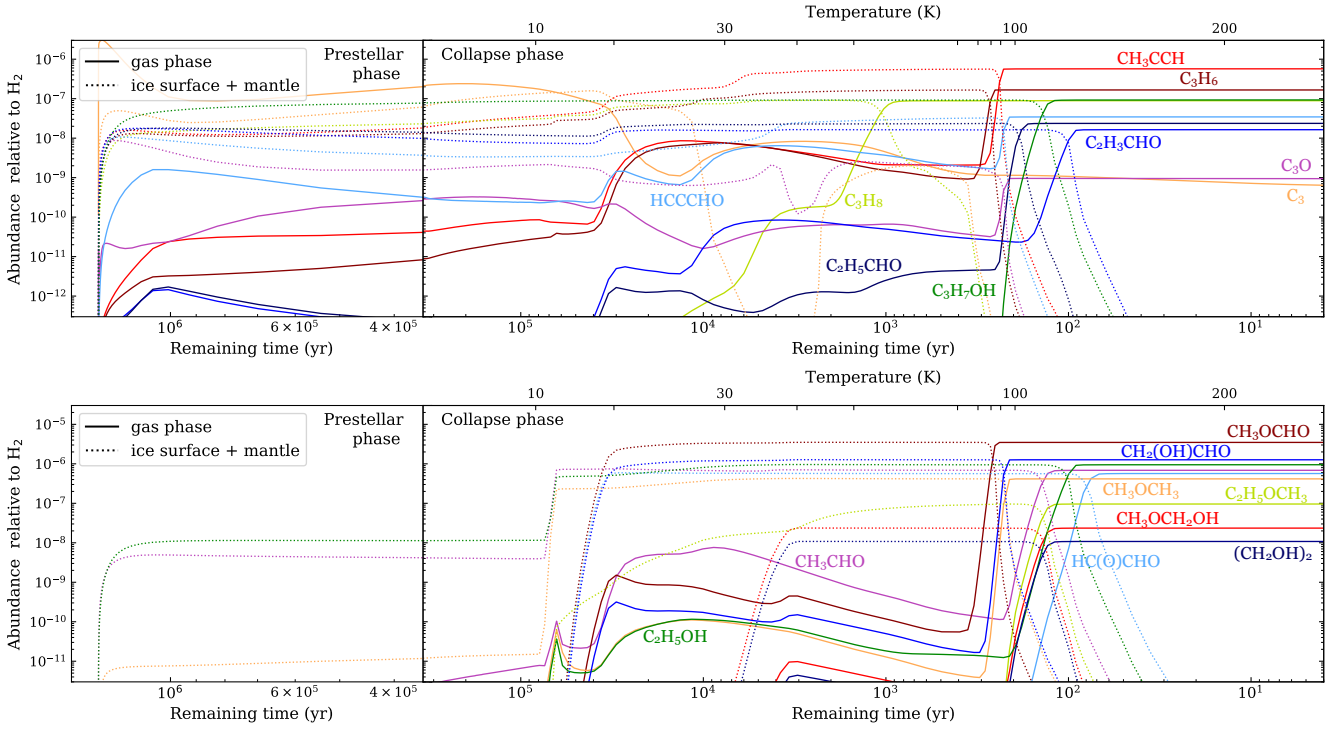


Fig. D.1. Evolution of the abundances of three-carbon species during the prestellar and the collapse phase of the simulation run A1. The time axis is reversed to better visualise the abundance evolution. Each color corresponds to a single species, with its abundance in the gas phase and on grain surfaces shown in solid and dotted lines, respectively.

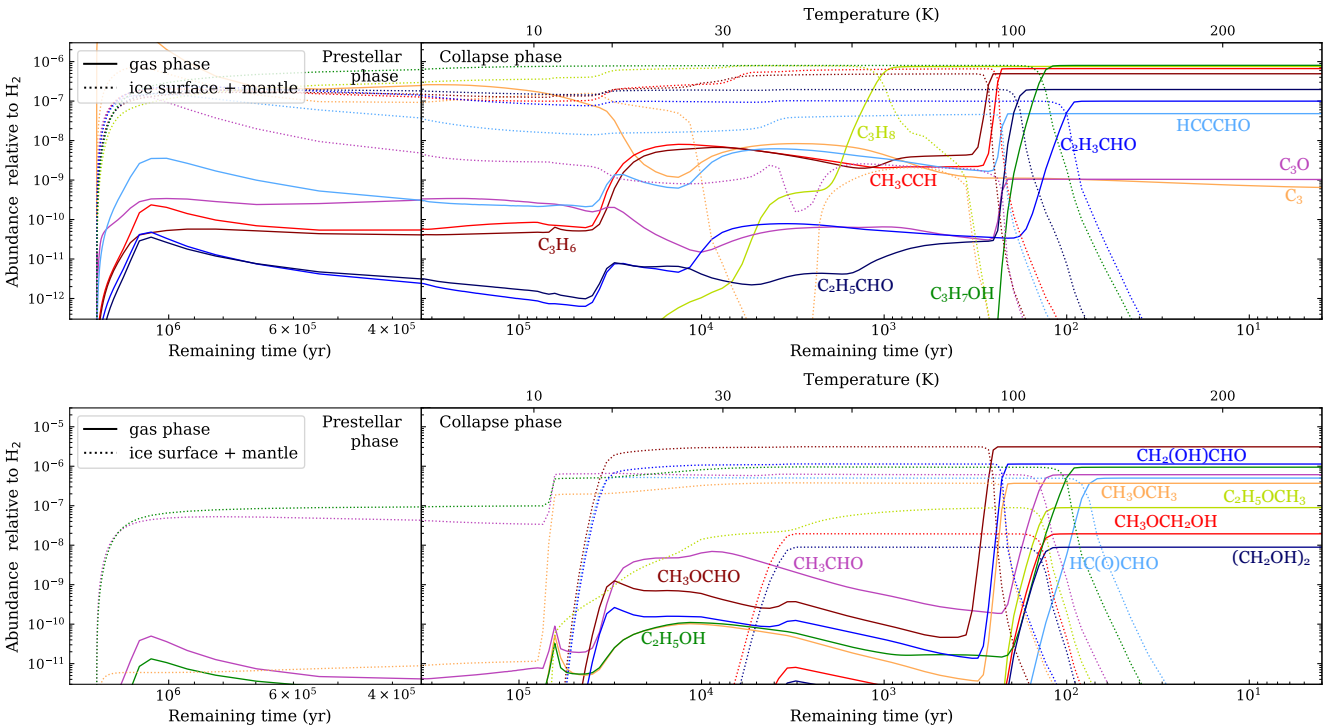


Fig. D.2. Evolution of the abundances of three-carbon species during the prestellar and the collapse phase of the simulation run A2. The time axis is reversed to better visualise the abundance evolution. Each color corresponds to a single species, with its abundance in the gas phase and on grain surfaces shown in solid and dotted lines, respectively.

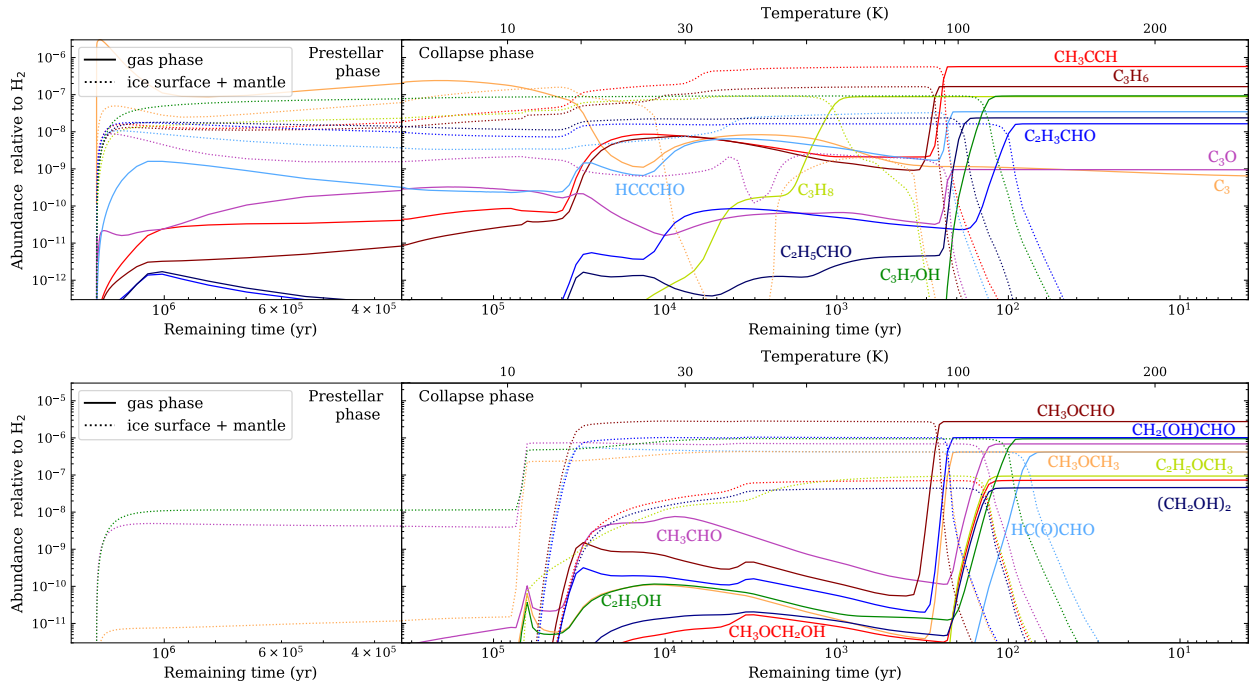


Fig. D.3. Evolution of the abundances of three-carbon species during the prestellar and the collapse phase of the simulation run B1. The time axis is reversed to better visualise the abundance evolution. Each color corresponds to a single species, with its abundance in the gas phase and on grain surfaces shown in solid and dotted lines, respectively.

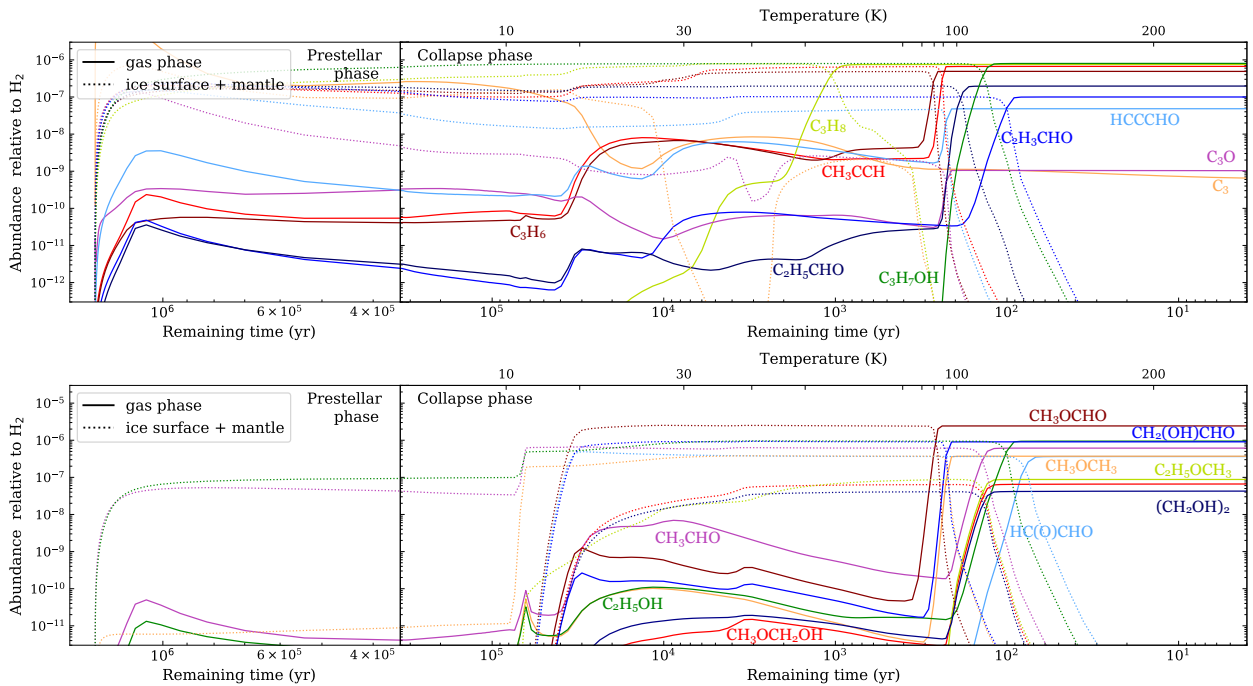


Fig. D.4. Evolution of the abundances of three-carbon species during the prestellar and the collapse phase of the simulation run B2. The time axis is reversed to better visualise the abundance evolution. Each color corresponds to a single species, with its abundance in the gas phase and on grain surfaces shown in solid and dotted lines, respectively.

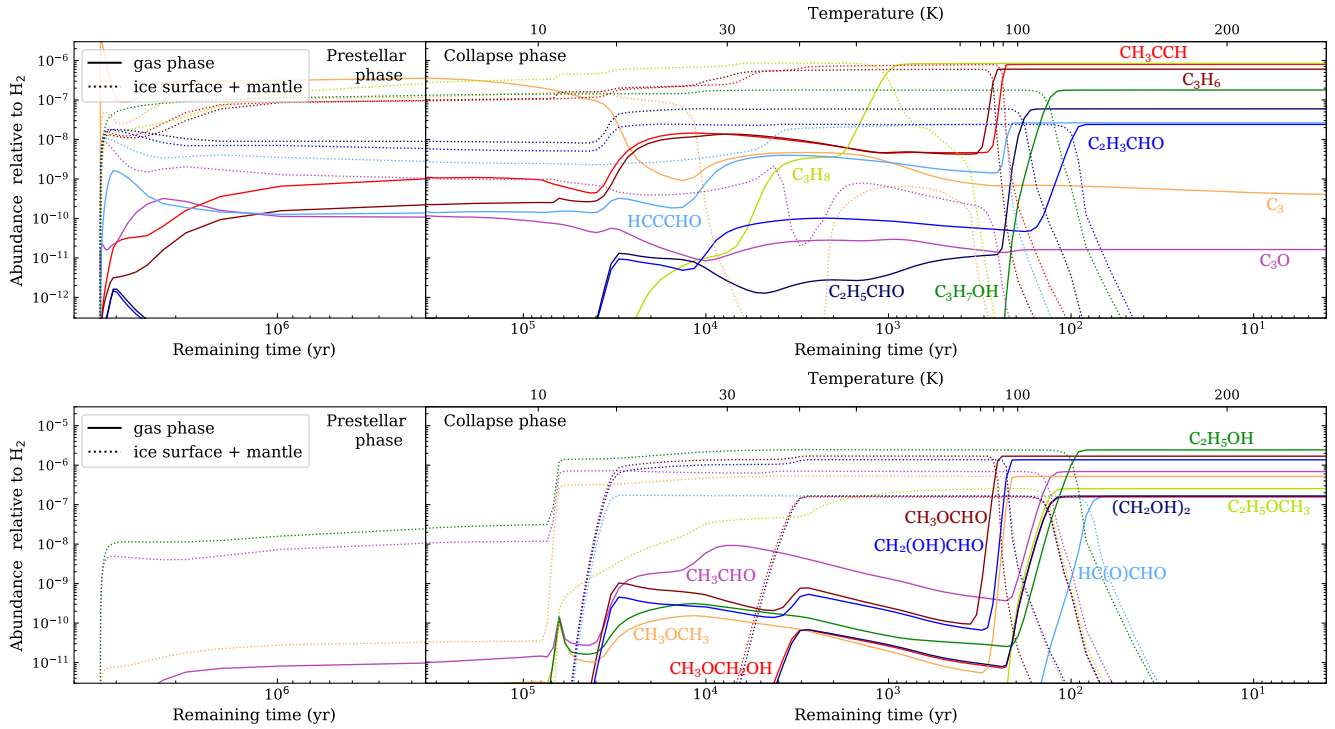


Fig. D.5. Evolution of the abundances of three-carbon species during the prestellar and the collapse phase of the simulation run C1. The time axis is reversed to better visualise the abundance evolution. Each color corresponds to a single species, with its abundance in the gas phase and on grain surfaces shown in solid and dotted lines, respectively.

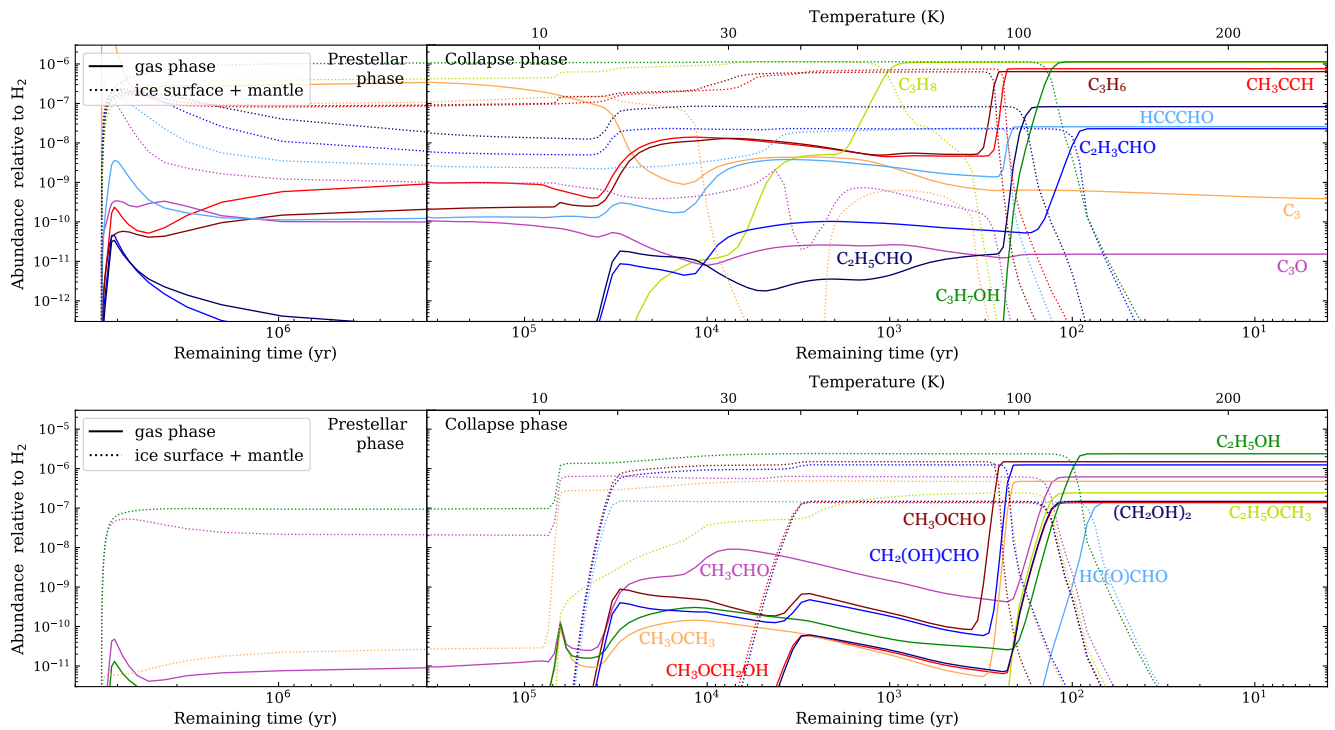


Fig. D.6. Evolution of the abundances of three-carbon species during the prestellar and the collapse phase of the simulation run C2. The time axis is reversed to better visualise the abundance evolution. Each color corresponds to a single species, with its abundance in the gas phase and on grain surfaces shown in solid and dotted lines, respectively.

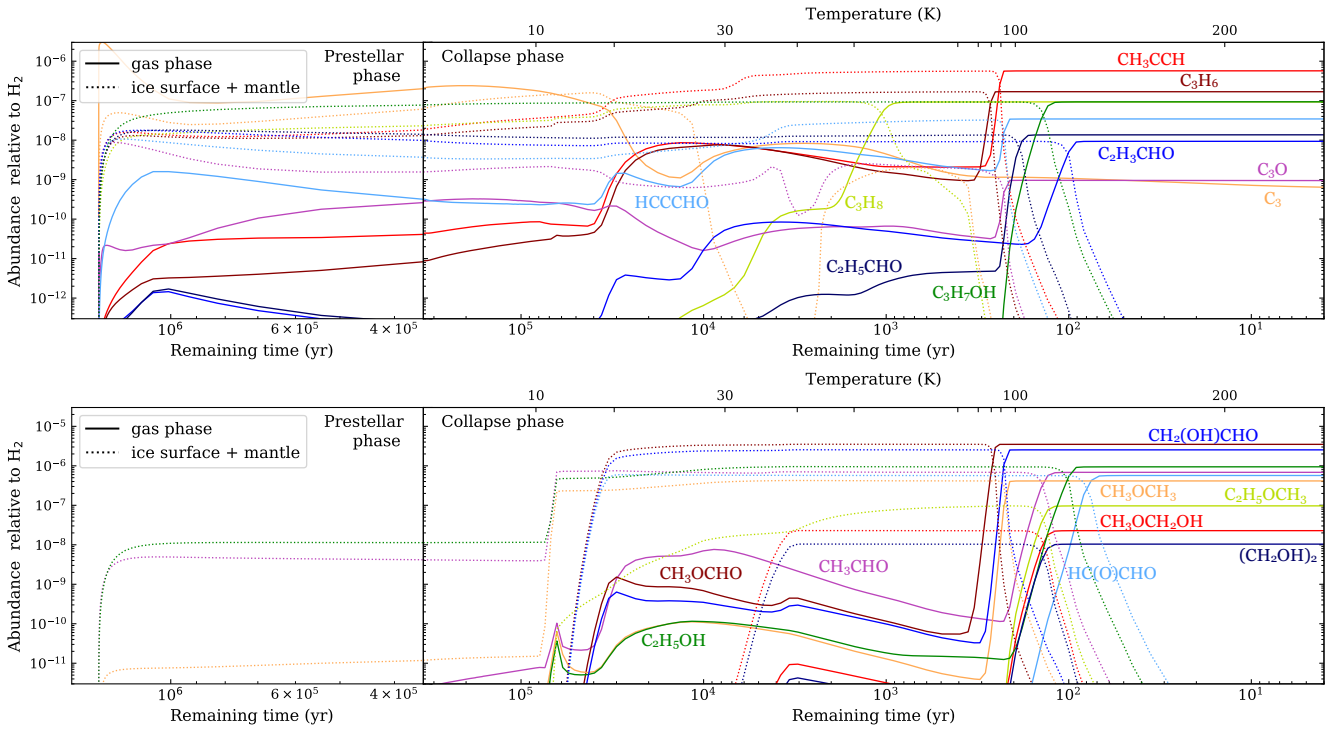


Fig. D.7. Evolution of the abundances of three-carbon species during the prestellar and the collapse phase of the simulation run D1. The time axis is reversed to better visualise the abundance evolution. Each color corresponds to a single species, with its abundance in the gas phase and on grain surfaces shown in solid and dotted lines, respectively.

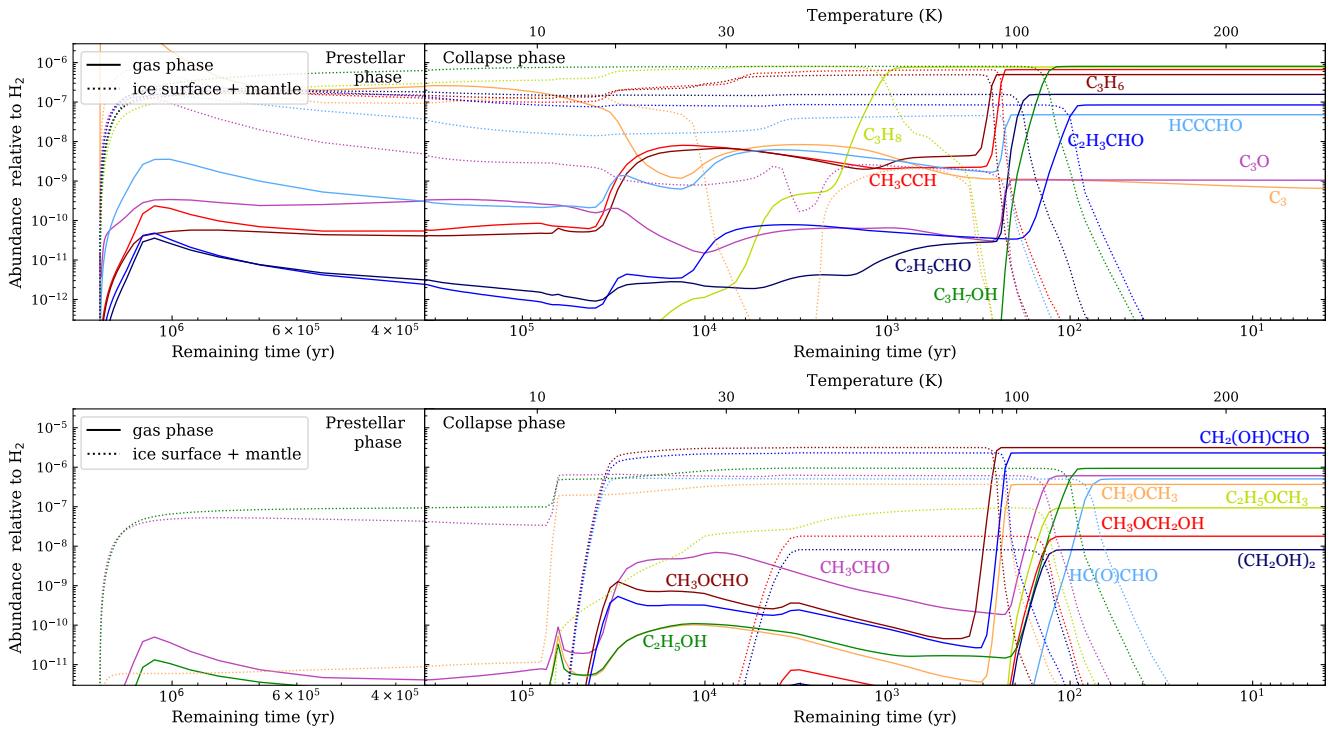


Fig. D.8. Evolution of the abundances of three-carbon species during the prestellar and the collapse phase of the simulation run D2. The time axis is reversed to better visualise the abundance evolution. Each color corresponds to a single species, with its abundance in the gas phase and on grain surfaces shown in solid and dotted lines, respectively.

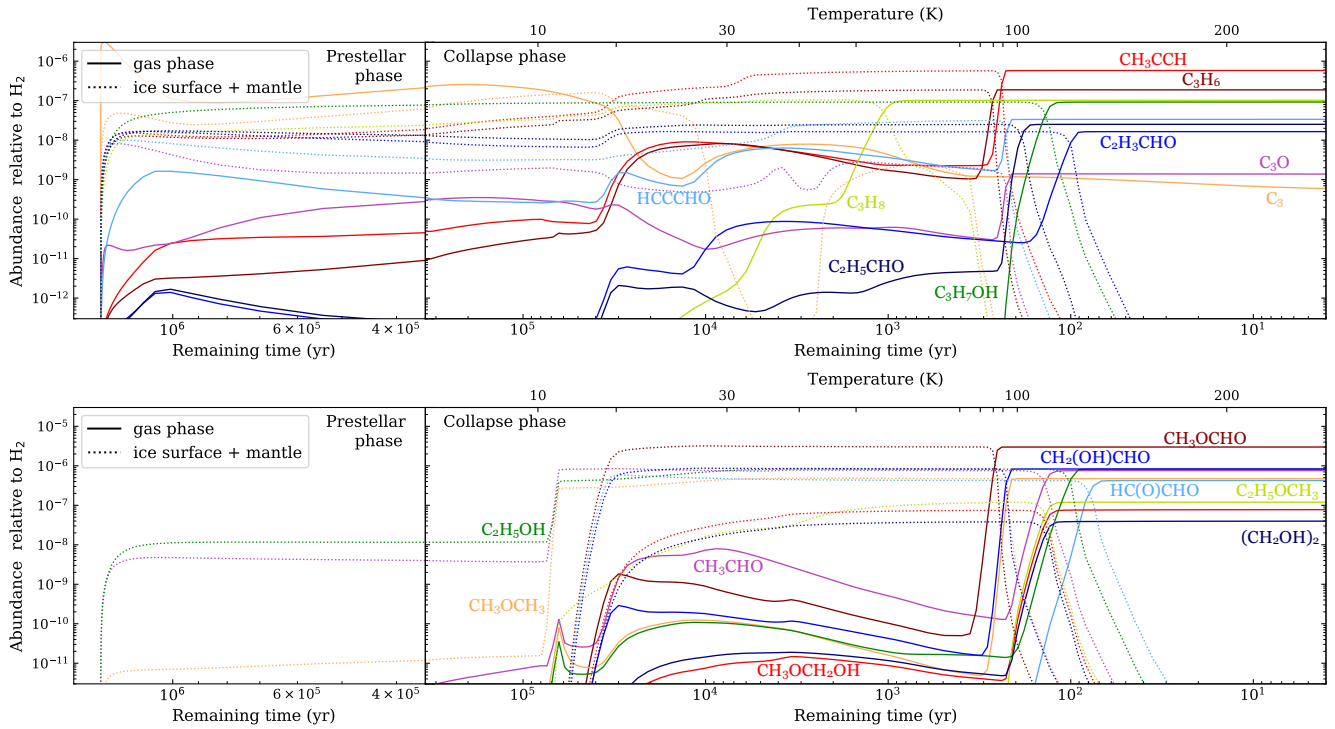


Fig. D.9. Evolution of the abundances of three-carbon species during the prestellar and the collapse phase of the simulation run E1. The time axis is reversed to better visualise the abundance evolution. Each color corresponds to a single species, with its abundance in the gas phase and on grain surfaces shown in solid and dotted lines, respectively.

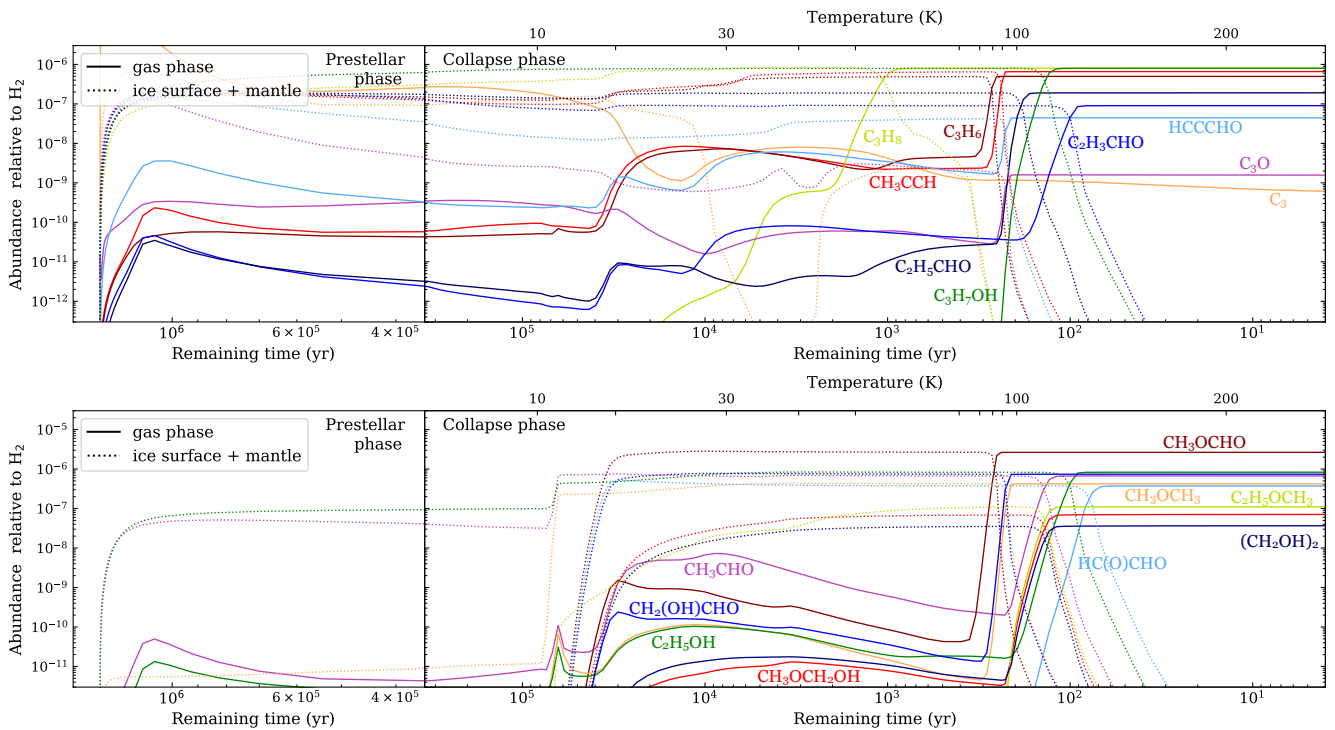


Fig. D.10. Evolution of the abundances of three-carbon species during the prestellar and the collapse phase of the simulation run E2. The time axis is reversed to better visualise the abundance evolution. Each color corresponds to a single species, with its abundance in the gas phase and on grain surfaces shown in solid and dotted lines, respectively.

Appendix E: C₂H₃CHO line list

This section lists, in Table E.1, the C₂H₃CHO transitions corresponding to the lines having an intensity above 3σ in the observations. The firmly detected transitions, which are optically thin and unblended in the conditions of the best fit, are annotated with the letter “Y”.

Table E.1. Line list of the observed C₂H₃CHO transitions above 3σ .

Transition $J(K_a, K_c)-J'(K'_a, K'_c)$	Fitted	ν (GHz)	g_u	E_u (K)	A_{ul} (s ⁻¹)
25(1,24)–24(1,23)	Y	225.1917	51	143	6.054×10^{-4}
27(0,27)–26(0,26)	Y	233.7577	55	159	6.788×10^{-4}
26(1,25)–25(1,24)		233.9402	53	154	6.793×10^{-4}
26(2,24)–25(2,23)	Y	235.9421	53	160	6.947×10^{-4}
27(10,17)–26(10,16)		240.4387	55	367	6.384×10^{-4}
27(10,18)–26(10,17)		240.4387	55	367	6.384×10^{-4}
27(9,18)–26(9,17)		240.4537	55	328	6.578×10^{-4}
27(9,19)–26(9,18)		240.4537	55	328	6.578×10^{-4}
27(8,19)–26(8,18)	Y	240.4793	55	293	6.752×10^{-4}
27(8,20)–26(8,19)	Y	240.4793	55	293	6.752×10^{-4}
27(7,21)–26(7,20)	Y	240.5217	55	262	6.908×10^{-4}
27(7,20)–26(7,19)	Y	240.5217	55	262	6.908×10^{-4}
27(6,22)–26(6,21)		240.5929	55	236	7.047×10^{-4}
27(6,21)–26(6,20)		240.5929	55	236	7.047×10^{-4}
28(2,27)–27(2,26)		247.4024	57	181	8.021×10^{-4}
29(0,29)–28(0,28)	Y	250.6283	59	182	8.377×10^{-4}
37(3,35)–36(3,34)		329.5826	75	319	1.902×10^{-3}
37(8,30)–36(8,29)		329.6375	75	432	1.826×10^{-3}
37(8,29)–36(8,28)		329.6375	75	432	1.826×10^{-3}
37(7,31)–36(7,30)	Y	329.7554	75	401	1.850×10^{-3}
37(7,30)–36(7,29)	Y	329.7554	75	401	1.850×10^{-3}
37(5,33)–36(5,32)		330.2566	75	352	1.892×10^{-3}
37(5,32)–36(5,31)		330.3155	75	352	1.893×10^{-3}
37(4,34)–36(4,33)	Y	330.5505	75	334	1.909×10^{-3}
37(4,33)–36(4,32)		331.4060	75	334	1.924×10^{-3}
38(2,37)–37(2,36)		333.8975	77	323	1.985×10^{-3}
37(3,34)–36(3,33)	Y	334.7764	75	321	1.994×10^{-3}
39(1,39)–38(1,38)		334.9111	79	325	2.008×10^{-3}
39(0,39)–38(0,38)	Y	335.0926	79	325	2.012×10^{-3}
37(2,35)–36(2,34)		335.4273	75	313	2.012×10^{-3}
38(1,37)–37(1,36)	Y	336.4730	77	322	2.032×10^{-3}
38(3,36)–37(3,35)		338.4007	77	336	2.060×10^{-3}
38(7,32)–37(7,31)		338.6860	77	418	2.008×10^{-3}
38(7,31)–37(7,30)		338.6860	77	418	2.008×10^{-3}
38(4,35)–37(4,34)		339.5117	77	350	2.071×10^{-3}
38(4,34)–37(4,33)		340.5275	77	351	2.089×10^{-3}
39(2,38)–38(2,37)		342.4848	79	339	2.143×10^{-3}
40(1,40)–39(1,39)		343.3917	81	342	2.166×10^{-3}
40(0,40)–39(0,39)	Y	343.5483	81	342	2.169×10^{-3}
38(3,35)–37(3,34)		344.0665	77	338	2.166×10^{-3}
38(2,36)–37(2,35)		344.2952	77	330	2.177×10^{-3}
39(1,38)–38(1,37)		344.8722	79	338	2.190×10^{-3}
39(3,37)–38(3,36)		347.2066	79	352	2.226×10^{-3}
39(8,32)–38(8,31)		347.4788	79	465	2.151×10^{-3}
39(8,31)–38(8,30)		347.4788	79	465	2.151×10^{-3}
39(7,33)–38(7,32)		347.6181	79	434	2.176×10^{-3}
39(7,32)–38(7,31)		347.6181	79	434	2.176×10^{-3}
41(1,41)–40(1,40)		351.8700	83	358	2.331×10^{-3}
41(0,41)–40(0,40)		352.0051	83	358	2.334×10^{-3}
39(2,37)–38(2,36)		353.1277	79	347	2.350×10^{-3}
40(1,39)–39(1,38)		353.2630	81	355	2.354×10^{-3}
39(3,36)–38(3,35)		353.3494	79	355	2.348×10^{-3}
40(3,38)–39(3,37)	Y	355.9997	81	369	2.401×10^{-3}
40(7,34)–39(7,33)		356.5518	81	451	2.353×10^{-3}

Table E.1. continued.

Transition $J(K_a, K_c)-J'(K'_a, K'_c)$	Fitted	ν (GHz)	g_u	E_u (K)	A_{ul} (s ⁻¹)
40(7,33)–39(7,32)		356.5518	81	451	2.353×10^{-3}
40(4,37)–39(4,36)	Y	357.4249	81	384	2.420×10^{-3}
41(2,40)–40(2,39)	Y	359.6292	83	373	2.483×10^{-3}
42(1,42)–41(1,41)		360.3463	85	376	2.504×10^{-3}
42(0,42)–41(0,41)		360.4625	85	376	2.506×10^{-3}
40(2,38)–39(2,37)		361.9237	81	364	2.531×10^{-3}
40(3,37)–39(3,36)		362.6215	81	372	2.539×10^{-3}

Appendix F: C₃H₆ line list

This section lists, in Table F.1, the C₃H₆ transitions corresponding to the lines having an intensity above 3σ in the observations. The firmly detected transitions, which are optically thin and unblended in the conditions of the best fit, are annotated with the letter “Y”.

Table F.1. Line list of the observed C₃H₆ transitions above 3σ .

Transition $J(K_a, K_c)-J'(K'_a, K'_c)$	Fitted	ν (GHz)	g_u	E_u (K)	A_{ul} (s ⁻¹)
13(2,12)–12(2,11) E		225.1013	108	83	1.517×10^{-5}
13(2,12)–12(2,11) A		225.1024	108	83	1.517×10^{-5}
13(1,12)–12(1,11) E		231.2205	108	80	1.672×10^{-5}
13(1,12)–12(1,11) A		231.2233	108	80	1.672×10^{-5}
13(2,11)–12(2,10) E		232.5859	108	85	1.676×10^{-5}
13(2,11)–12(2,10) A		232.5869	108	85	1.676×10^{-5}
14(0,14)–13(0,13) E	Y	235.2697	116	86	1.772×10^{-5}
14(0,14)–13(0,13) A	Y	235.2714	116	86	1.772×10^{-5}
19(1,18)–18(1,17) E	Y	331.5709	156	164	4.986×10^{-5}
19(1,18)–18(1,17) A	Y	331.5751	156	164	4.986×10^{-5}
20(1,20)–19(1,19) E		331.7410	164	170	5.023×10^{-5}
20(1,20)–19(1,19) A		331.7421	164	170	5.024×10^{-5}
19(8,11)–18(8,10) E		331.8207	156	274	4.148×10^{-5}
19(8,12)–18(8,11) A		331.8207	156	274	4.148×10^{-5}
19(8,11)–18(8,10) A		331.8207	156	274	4.148×10^{-5}
19(7,13)–18(7,12) A		331.9592	156	248	4.363×10^{-5}
19(7,12)–18(7,11) A		331.9592	156	248	4.363×10^{-5}
19(3,17)–18(3,16) E	Y	332.1087	156	176	4.926×10^{-5}
19(3,17)–18(3,16) A	Y	332.1091	156	176	4.926×10^{-5}
19(6,14)–18(6,13) A		332.1877	156	224	4.554×10^{-5}
19(6,13)–18(6,12) A		332.1890	156	224	4.554×10^{-5}
20(0,20)–19(0,19) E		332.1893	164	170	5.045×10^{-5}
20(0,20)–19(0,19) A		332.1909	164	170	5.045×10^{-5}
19(6,14)–18(6,13) E		332.1909	156	224	4.548×10^{-5}
19(6,13)–18(6,12) E		332.1909	156	224	4.548×10^{-5}
19(5,15)–18(5,14) A		332.5731	156	204	4.724×10^{-5}
19(5,15)–18(5,14) E		332.5773	156	204	4.674×10^{-5}
19(5,14)–18(5,13) A		332.6150	156	204	4.726×10^{-5}
19(5,14)–18(5,13) E		332.6154	156	204	4.676×10^{-5}
19(4,16)–18(4,15) A		333.0380	156	188	4.871×10^{-5}
19(4,16)–18(4,15) E		333.0396	156	188	4.870×10^{-5}
19(4,15)–18(4,14) A		333.7945	156	188	4.904×10^{-5}
19(4,15)–18(4,14) E		333.7959	156	188	4.904×10^{-5}
19(3,16)–18(3,15) A		338.1148	156	177	5.202×10^{-5}
19(3,16)–18(3,15) E		338.1152	156	177	5.202×10^{-5}
19(2,17)–18(2,16) E	Y	340.8266	156	170	5.403×10^{-5}
19(2,17)–18(2,16) A	Y	340.8293	156	170	5.403×10^{-5}
20(2,19)–19(2,18) E		343.0971	164	181	5.512×10^{-5}
20(2,19)–19(2,18) A		343.0990	164	181	5.512×10^{-5}

Table F.1. continued.

Transition $J(K_a, K_c) - J'(K'_a, K'_c)$	Fitted	ν (GHz)	g_u	E_u (K)	A_{ul} (s ⁻¹)
20(1,19)–19(1,18) E	Y	347.7734	164	180	5.760×10^{-5}
20(1,19)–19(1,18) A	Y	347.7777	164	180	5.760×10^{-5}
21(1,21)–20(1,20) E		348.0323	172	187	5.809×10^{-5}
21(1,21)–20(1,20) A		348.0335	172	187	5.809×10^{-5}
21(0,21)–20(0,20) E	Y	348.3802	172	187	5.827×10^{-5}
21(0,21)–20(0,20) A		348.3815	172	187	5.827×10^{-5}
20(10,11)–19(10,10) E	Y	349.1524	164	356	4.411×10^{-5}
20(10,11)–19(10,10) A	Y	349.1526	164	356	4.412×10^{-5}
20(10,10)–19(10,9) A	Y	349.1526	164	356	4.412×10^{-5}
20(8,13)–19(8,12) A		349.3206	164	291	4.948×10^{-5}
20(8,12)–19(8,11) A		349.3206	164	291	4.948×10^{-5}
20(8,12)–19(8,11) E		349.3206	164	291	4.948×10^{-5}
20(3,18)–19(3,17) E		349.4123	164	192	5.757×10^{-5}
20(3,18)–19(3,17) A		349.4129	164	192	5.757×10^{-5}
20(7,14)–19(7,13) A	Y	349.4842	164	264	5.176×10^{-5}
20(7,13)–19(7,12) A	Y	349.4843	164	264	5.176×10^{-5}
20(6,15)–19(6,14) A		349.7525	164	241	5.379×10^{-5}
20(6,14)–19(6,13) A		349.7549	164	241	5.379×10^{-5}
20(6,15)–19(6,14) E		349.7561	164	241	5.358×10^{-5}
20(6,14)–19(6,13) E		349.7568	164	241	5.358×10^{-5}
20(5,16)–19(5,15) A		350.1976	164	221	5.563×10^{-5}
20(5,16)–19(5,15) E		350.2011	164	221	5.542×10^{-5}
20(5,15)–19(5,14) A	Y	350.2639	164	221	5.567×10^{-5}
20(5,15)–19(5,14) E	Y	350.2653	164	221	5.545×10^{-5}
20(4,17)–19(4,16) A		350.6713	164	205	5.720×10^{-5}
20(4,17)–19(4,16) E		350.6728	164	205	5.720×10^{-5}
20(4,16)–19(4,15) A	Y	351.7358	164	205	5.772×10^{-5}
20(4,16)–19(4,15) E	Y	351.7372	164	205	5.772×10^{-5}
20(3,17)–19(3,16) A	Y	356.6568	164	194	6.130×10^{-5}
20(3,17)–19(3,16) E	Y	356.6571	164	194	6.130×10^{-5}
20(2,18)–19(2,17) E		358.4284	164	187	6.296×10^{-5}
20(2,18)–19(2,17) A		358.4315	164	187	6.298×10^{-5}
21(2,20)–20(2,19) E		359.7217	172	199	6.365×10^{-5}
21(2,20)–20(2,19) A		359.7237	172	199	6.365×10^{-5}